Hydration mechanism in Earth’s mantle transition zone investigated by neutron diffraction

2017, March
Narangoo PUREVJAV

Graduate School of
Natural Science and Technology
(Doctor’s Course)
Institute for Planetary Materials
OKAYAMA UNIVERSITY

ABSTRACT

Water plays a crucial role for the evolution of Earth and planets. It exists as liquid state on the Earth's surface but also exists as hydroxyls within solid hydrous minerals in the Earth's deep interior. The budget of the latter type of water is controversial. The surface liquid water is transported into the deep interior by subducting oceanic slabs. The transported amount of water is much larger than that returning to the surface by magmatism. By previous experimental studies, it has been shown that some of the Earth's mantle minerals can uptake water within their structures. Mantle transition zone at depths from 410 to 660 km is considered to be the largest reservoir of such water within the bulk Earth, which mainly consists of wadsleyite and ringwoodite mineral phases. It is because these minerals were proved to uptake at most 3 wt.% water in their crystal structures, which is their exclusive property compared with the other upper and lower mantle constituent minerals. Recently, it was demonstrated that a ringwoodite crystal of terrestrial origin was containing around 1.4 wt.% of water. If we assume that the whole lower mantle transition zone is as wet as this ringwoodite, its water is equal with the total mass of the all oceans. By seismological studies, it was revealed that anomalous low-velocity regions existed at the top and the bottom of the mantle transition zone, which can be the results of hydration and dehydration of hydrous wadsleyite and hydrous ringwoodite, respectively.

Water shows significant effects on the physical properties of wadsleyite and ringwoodite such as increasing their electrical conductivity, reducing their elasticity, and shifting their phase boundary. In order to understand the effect of water on these properties, hydrogen sites and hydration mechanisms need to be understood in the relevant structures. Thus, here we investigate the hydrated structures of the two mantle transition zone minerals by neutron diffraction. It is the most straightforward technique probing hydrogen in condensed matter. This is because neutron directly interacts with atomic nuclei. In the case of hydrogen,

it can be observed as clear as the other heavy atoms. We conducted time-of-flight (TOF) powder and single-crystal neutron diffraction for analyzing the structures of hydrous ringwoodite and hydrous wadsleyite. Through the syntheses experiments, we newly developed two cell assemblies, which were suitable for synthesizing the required quality of the samples. The successfully recovered powder and single crystal samples were fully characterized for evaluating their chemical homogeneity and crystallinity prior to the neutron diffraction measurements. The synthesis and characterization procedures are shown in Chapter II.

We conducted TOF powder neutron diffraction measurement for deuterated (D_2O-bearing) ringwoodite at room temperature. The measurement was carried out at Japan Proton Accelerator Research Complex. The obtained diffraction pattern was with sufficient peak intensities and with exceptionally low and flat background. Continuing after this study, we conducted the TOF Laue single-crystal neutron diffraction measurements for hydrogenated (H_2O-bearing) ringwoodite and hydrogenated wadsleyite. The diffraction datasets were obtained at Oak Ridge National Laboratory. This method is even more suitable to accurately refine the crystal structures because of its much higher spatial resolution than that of powder diffraction. It is applicable even for the samples involving light hydrogen. These measurements were also motivated for observing the possible differences between the two structures involving the two different hydrogen isotopes (deuterium and hydrogen). An iron-free hydrous ringwoodite crystal with 600 μm in size was measured at 100 K. An iron-free hydrous wadsleyite crystal with 800 μm in size was measured at 100 K and 295 K. These all procedures of neutron diffraction measurements are shown in Chapter III. Obtained neutron diffraction datasets were successfully analysed for refining hydrogen (deuterium) sites and occupancies in the crystal structures of hydrous ringwoodite and hydrous wadsleyite. The procedures of structure analyses are explained in Chapter IV.

By powder neutron diffraction study of deuterated ringwoodite, we demonstrated that the deuterium atoms simultaneously exchanged with magnesium, iron and silicon cations, which were occupying both of octahedral and tetrahedral sites in the ringwoodite crystal structure. By subsequent single-crystal neutron diffraction study, we clearly observed that hydrogen atoms were exchanged with magnesium cation in octahedral sites, while we could not refine hydrogen atoms in tetrahedral sites. However, significant occupancy deficiency of silicon was observed in the tetrahedral site, which strongly suggested that hydrogen must also be exchanged with silicon cations, in addition to the magnesium cations. This result is consistent with the powder neutron diffraction result of the iron-bearing deuterated ringwoodite. We also found that the hydrogenated octahedron in H_2O-bearing ringwoodite had larger volume than that of the deuterated octahedron in D_2O-bearing ringwoodite. These results and discussion on ringwoodite are shown in Chapter V.

By single-crystal neutron diffraction study of hydrogenated wadsleyite, we demonstrated that hydrogen in wadsleyite exchanged only with magnesium cation at M3 octahedral site, while it did not exchange with magnesium cation at the other M sites or silicon cation at T site. In addition, we also refined occupancies of the other cations at every sites, where except for the magnesium at M3 site all cations had full occupancies. Considering these results, we discuss the unique potential of single-crystal neutron diffraction for quantitative analysis of H_2O concentration in hydrous minerals. These results and discussion on wadsleyite are shown in Chapter VI.

Comparing the results of hydrous ringwoodite with hydrous wadsleyite, we demonstrated that hydration mechanisms between these two mineral phases are qualitatively different each other. Thus we conclude that differences in physical properties between hydrous ringwoodite and hydrous wadsleyite are mainly induced by their distinct hydration mechanisms in their crystal structures. We especially focus on discussion about the bulk moduli sensitivity against water concentration for these two minerals. The details of these discussions are shown in Chapter VII. The conclusions of these Ph.D studies are shown in Chapter VIII.

TABLE OF CONTENTS

II. Syntheses and evaluations of transition zone minerals subject for neutron

II.3.2. Experimental conditions

II.4. Evaluation of recovered samples

III. Neutron diffraction

III.2. Data collection procedures

IV. Structure analysis

IV.2. Powder and single-crystal neutron diffraction data analyses

V. Hydration mechanism of ringwoodite

V.2. Results

VI. Hydration mechanism of wadsleyite

VII. Water in mantle transition zone

I. INTRODUCTION

I. Introduction

Water plays a crucial role for the evolution of the Earth and planets. It not only presents on the surface of the Earth as oceans, but also presents in its interior as structurally-bound hydrogen within minerals. Evidence from seismological and mineralogical studies increasingly indicates that water from the oceans has been transported into the deep Earth by subduction of oceanic slabs (Figure 1.1). Peacock [1990] estimated that the amount of transported water by subducting slab is 8.7 x 10^{11}kg/yr, which is generally consistent with the other studies [*Bebout*, 1996; *Ito et al.*, 1983]. However, the back-transported amount of water by magmatism is 2 x 10^{11}kg/yr, which is by far smaller than that of transported amount to the mantle [*Bebout*, 1996; *Peacock*, 1990]. Where is the remaining subducted water? The most possible hypothesis is that the water is stored in the deep mantle minerals. Especially, minerals in mantle transition zone (MTZ) are considered to be the most dominant reservoirs of transported water from the surface [*Bercovici and Karato*, 2003; *Inoue et al.*, 1995; *Ohtani et al.*, 2004; *Smyth*, 1987]. The MTZ is located in the deeper portion of the upper mantle between approximately 410 and 660 km depth. It is characterized by rapid increase of seismic wave velocities with depth [*Benz and Vidale*, 1993; *Dziewonski and Anderson*, 1981; *Shearer*, 1990] (Figure 1.2a).

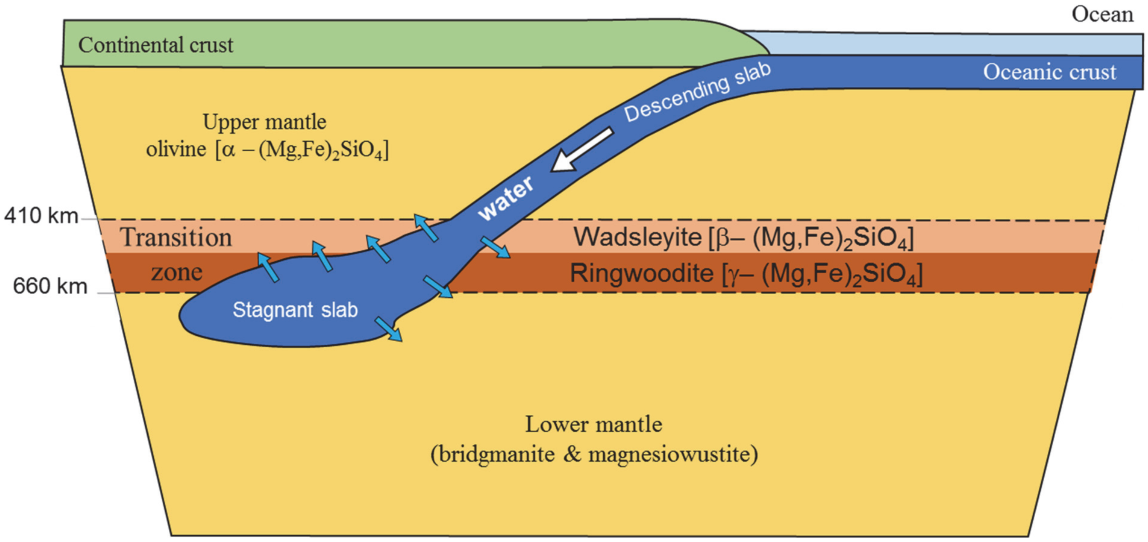

Figure1.1. A sketch of water transportation in the mantle.

Origins of these discontinuities are ascribed to three successive phase transformations, which include those from olivine [α – (Mg, Fe^{2+})$_2$SiO$_4$] to its denser polymorph, wadsleyite [β – (Mg, Fe^{2+})$_2$SiO$_4$] at around 410 km, and from wadsleyite to ringwoodite [γ – (Mg, Fe^{2+})$_2$SiO$_4$] at around 525 km (Figure 1.2b), and finally from ringwoodite to bridgmanite [(Mg,Fe)SiO$_3$] and magnesiowustite [(Mg,Fe)O] at around 660 km [*Akaogi et al.*, 1989; *Katsura and Ito*, 1989; *Morishima et al.*, 1994].

The MTZ mainly consists of wadsleyite and ringwoodite, which are the two denser high pressure polymorphs of olivine (Figure 1.3). These three polymorphs are all nominally anhydrous, while by experimental studies it was confirmed that wadsleyite and ringwoodite can absorb significant amount of structurally-bound hydrogen in their crystal structures. It was

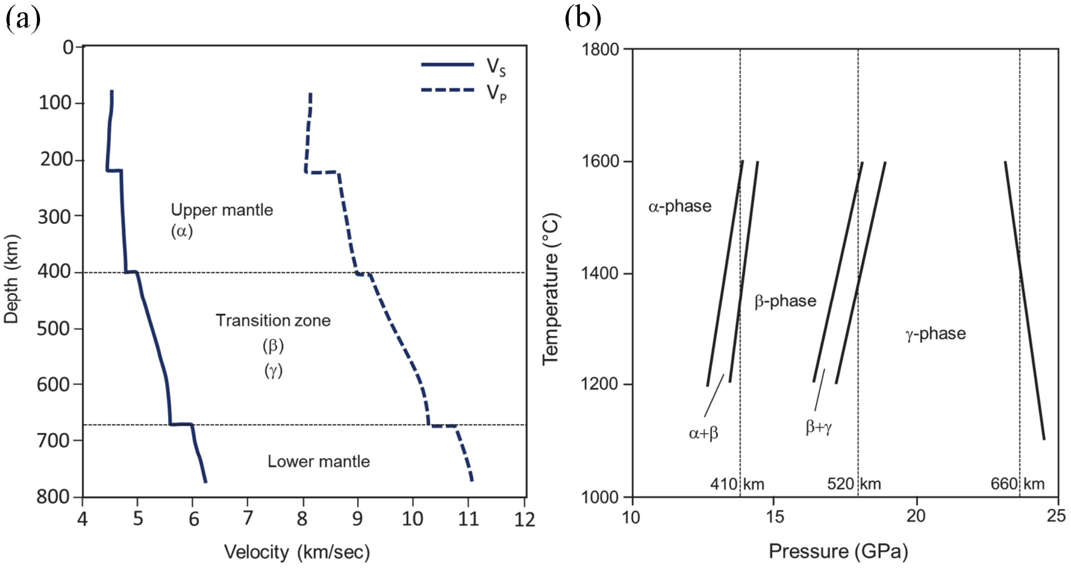

Figure 1.2. (a) Seismic velocity profile of mantle up to 800 km [*Dziewonski and Anderson*, 1981], Vs is shear wave velocity and Vp is compressional wave velocity. (b) Pressure-temperature phase diagram for Fo$_{90}$ after data from [*Katsura and Ito*, 1989] and [*Ito and Takahashi*, 1989].

reported that olivine can involve up to 1 wt.% of water as structurally-bound hydrogen [*Smyth et al.*, 2006], while wadsleyite and ringwoodite can involve up to 3 wt.% of water as the hydrogen in their crystal structures in relevant MTZ conditions [*Inoue et al.*, 1995; *Kohlstedt et al.*, 1996; *Kudoh et al.*, 1996; *Ye et al.*, 2012]. Expectation of such wet MTZ has been confirmed in part by the discovery of natural hydrous ringwoodite containing 1.4 wt. % of H_2O as an inclusion in diamond [*Pearson et al.*, 2014]. If we assume that the lower MTZ is storing such an amount of water, it is almost equal to all the mass of oceans [*Keppler*, 2014]. Moreover, it was proposed by previous seismological studies that some regions of the uppermost MTZ, at approximately 410 km depth, had anomalously lower velocities, which were suggested as partially molten regions generated by dehydration of subducted materials [*Revenaugh and Sipkin*, 1994; *Song et al.*, 2004; *van der Meijde et al.*, 2003]. At this depth, olivine transforms into wadsleyite, and is then able to be hydrated. Very recently it was proposed that a large

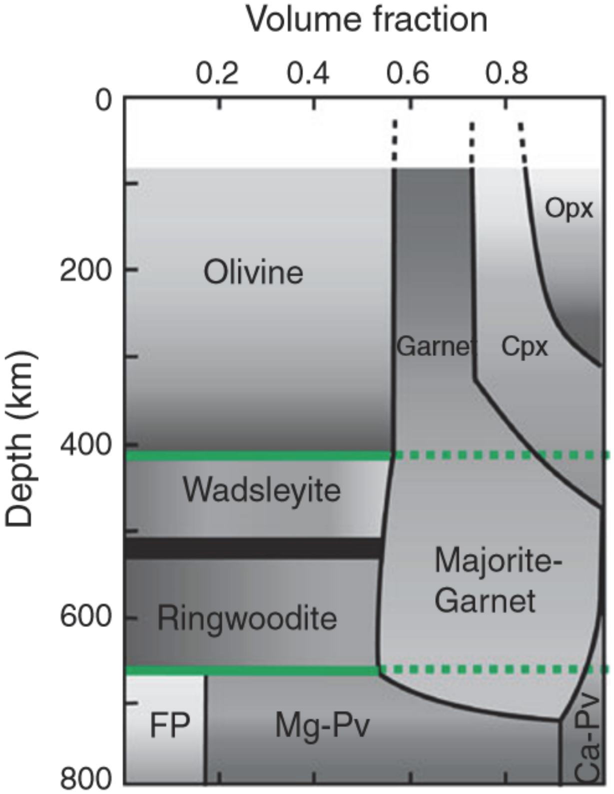

Figure 1.3. Mineral volume fraction for the top 800 km of mantle [*Pommier*, 2014].

region of the lowermost MTZ, around 660 km depth, is so extensively hydrated that it is capable of inducing dehydration melting [*Schmandt et al.*, 2014]. At this depth, wet ringwoodite decomposes to hydrous melt, bridgmanite and magnesiowustite. However, how much amount of water is being kept in MTZ is still unclear in a quantitative manner. By number of experimental studies, it has been confirmed that water shows significant influences on the physical properties of wadsleyite and ringwoodite such as increasing their thermal expansibility [*Inoue et al.*, 2004; *Ye et al.*, 2009; *Ye et al.*, 2012] and compressibility [*Holl et al.*, 2008; *Smyth et al.*, 2004; *Yusa et al.*, 2000], reducing their elastic moduli [*Chang et al.*, 2015; *Inoue et al.*, 1998; *Jacobsen et al.*, 2004; *Mao et al.*, 2011; *Mao et al.*, 2012] and increasing their electrical conductivities [*Dai and Karato*, 2009; *Huang et al.*, 2005; *Yoshino et al.*, 2008]. Wadsleyite and ringwoodite have similar crystal structures, because both of the structures consist of the cubic closest packing of oxygen atoms. These structures contain 56 atoms in their unit cells, respectively, in their dry forms. There are two types of polyhedra in their structures, which are octahedra and tetrahedra made of six and four oxygen anions, respectively. The octahedra (M sites) are filled by magnesium (Mg^{2+}) or iron (Fe^{2+}) cations, while the tetrahedra (T sites) are filled by silicon (Si^{4+}) cations (Figure 1.4). It is interesting to note that the crystal structures of wadsleyite and ringwoodite almost remain as original even after absorbing H_2O [*Kudoh et al.*, 1996; *Kudoh et al.*, 2000; *Sano-Furukawa et al.*, 2011; *Tsuchiya and Tsuchiya*, 2009]. By previous spectroscopic and first principle calculation works of nominally anhydrous minerals, it was reported that hydrogen (H) cations exchanged with magnesium (Mg^{2+}), iron (Fe^{2+}) and silicon (Si^{4+}) cations in the structures [*Blanchard et al.*, 2005; *Jacobsen et al.*, 2005; *Kohn et al.*, 2002; *Lemaire et al.*, 2004; *Walker et al.*, 2006]. These exchanging reactions were expected to occur while keeping total cation charge balances at M and T sites. Then, two hydrogen cations are expected to exchange with one Mg^{2+} or Fe^{2+} at M sites, while four hydrogen cations are expected to exchange with one Si^{4+} at T sites. It has been proposed that predominant hydration reaction occurs in M site in wadsleyite and ringwoodite structures, while minor hydration in T site may occur in ringwoodite involving more than 2 wt.% of water [*Ye et al.*, 2012].

Existence of structurally-bound hydrogen was independently confirmed by Raman, Infrared (IR) and Nuclear Magnetic Resonance (NMR) spectroscopies for both of wadsleyite and ringwoodite in their hydrated forms [*Ashbrook et al.*, 2005; *Griffin et al.*, 2013; *Jacobsen et al.*, 2005; *Stebbins et al.*, 2009; *Thomas et al.*, 2015; *Young et al.*, 1993], which are sensitive methods for analysing the local structures around hydrogen. On the other hand, general crystal structures of hydrous wadsleyite and hydrous ringwoodite were analysed by x-ray diffraction [*Kudoh et al.*, 1996; *Kudoh et al.*, 2000; *Smyth et al.*, 2003], while x-ray is not sensitive for light atoms such as hydrogen. This is because x-ray only interacts with electrons. First principle calculations were also carried out for hydrous wadsleyite and hydrous ringwoodite in order to resolve their hydrated structures [*Blanchard et al.*, 2009; *Blanchard et al.*, 2013; *Li et al.*, 2009; *Panero*, 2010; *Tsuchiya and Tsuchiya*, 2009]. However, these studies were not conclusive for the positions of hydrogen and its bonding geometries in the structures of wadsleyite and

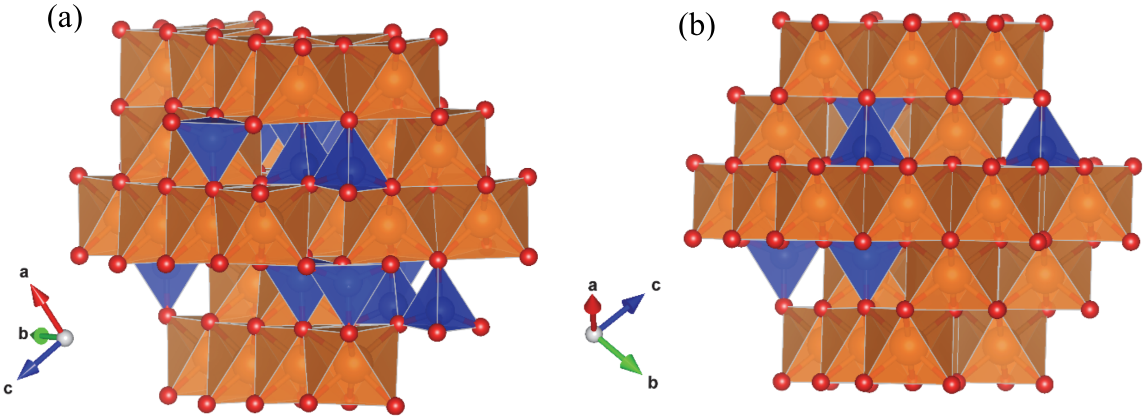

Wadsleyite (β)

Ringwoodite (γ)

Figure 1.4. (a) Wadsleyite with modified spinel structure (*Imma*). (b) Ringwoodite with cubic spinel structure ($Fd\bar{3}m$). M sites are shown in orange and T sites are shown in blue. These are drawn by VESTA [*Momma and Izumi*, 2011].

ringwoodite. There was no direct observation for analysing such local structures of the structurally-bound hydrogen in wadsleyite and ringwoodite, except just one work by using powder neutron diffraction on deuterated wadsleyite [*Sano-Furukawa et al.*, 2011].

Here I discuss about a few examples of influences of the structurally-bound hydrogen on physical properties of wadsleyite and ringwoodite. First, we discuss about relative molar volume against water concentrations (Figure 1.5). It is clear that volume expansion rate of ringwoodite by hydration is significantly larger than those of wadsleyite and olivine. Another example is elastic constants against water concentrations (Figure 1.6). Elastic constants of olivine, wadsleyite and ringwoodite are monotonically decreasing with increasing their water concentrations, which was observed by laboratory experiments [*Chang et al.*, 2015; *Inoue et al.*, 1998; *Jacobsen et al.*, 2008]. These property changes imply that the structurally-bound hydrogen atoms soften their structures by weakening their chemical bonds. If the weakening of their chemical bonds occur at the same location in these minerals structures, we should observe comparable slope of bulk moduli reduction against water concentration. However, it

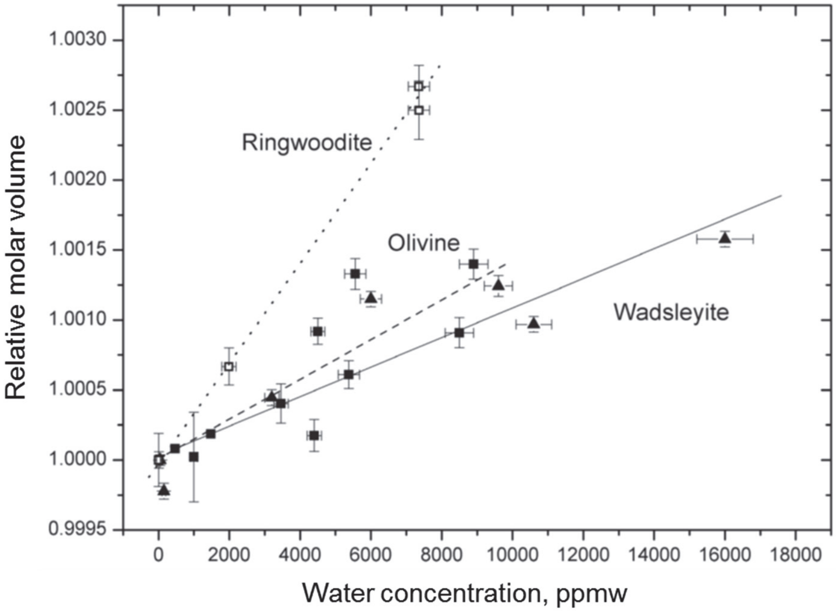

Figure 1.5. Relative molar volume expansion at ambient condition after hydration of olivine, wadsleyite, and ringwoodite [*Smyth and Jacobsen*, 2006].

is clear that the slope of bulk moduli in ringwoodite is relatively steeper than those of wadsleyite and olivine. It suggests that the weakening of chemical bonds must have distinct geometries among crystal structures of olivine, wadsleyite and ringwoodite. Therefore, hydrogen exchange reactions with the other cations are expected to be different in these minerals.

As mentioned above some part of the MTZ region consisting of hydrated wadsleyite and ringwoodite must have higher compressibility, which can be seismologically discriminated by their lower seismic velocities, at least in the uppermost or the lowermost MTZ. However, their water concentrations still remain very difficult to be estimated. This difficulty is partly because the degree of elastic constant reduction induced by hydration is strongly dependent on the exchanging cation species (Mg^{2+}, Fe^{2+} or Si^{4+}) with H^+ [*Panero*, 2010; *Tsuchiya and Tsuchiya*, 2009]. Additionally, the elastic constants of wadsleyite and ringwoodite were reported to have different sensitivities against unit concentration of water, even though the two

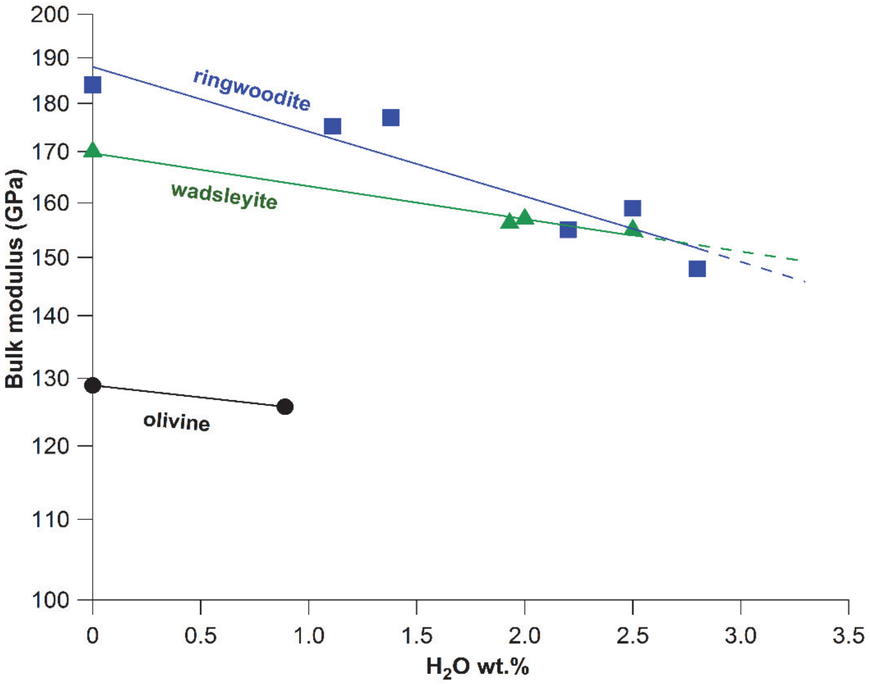

Figure 1.6. Effect of hydration on isothermal bulk modulus at ambient conditions for olivine, wadsleyite, and ringwoodite. The bulk moduli values are shown in log scale. The data points were taken from previous experimental works [*Hazen*, 1993; *Mao et al.*, 2011; *Mao et al.*, 2012; *Ye et al.*, 2012; *Yusa et al.*, 2000; *Zha et al.*, 1997].

minerals have very similar structures in their dry forms [*Mao et al.*, 2012; *Yusa et al.*, 2000]. Thus, again here we propose that hydrated crystal structures of wadsleyite and ringwoodite must be different in each other, especially their hydrogen sites and hydration exchange reactions with other cations. In other words, the chemical bonding in hydrous wadsleyite and hydrous ringwoodite should be softened at different positions in their crystal structures.

In order to confirm this hypothesis and also to evaluate the proposed hydrated structure models by theoretical works, here we analyse hydrogen sites and occupancies in both of wadsleyite and ringwoodite crystal structures by means of neutron diffraction. Neutron diffraction is the most straightforward way to analyze position of hydrogen in the crystal structures, because neutron interacts with the nuclei of atoms to be sensitive enough for light atoms such as hydrogen. Previously, deuterium (heavy hydrogen isotope – D) site position in wadsleyite was analysed by means of powder neutron diffraction [*Sano-Furukawa et al.*, 2011], while there was no relevant study on hydrous ringwoodite. Thus, as a part of this Ph.D thesis, we conducted powder neutron diffraction on deuterated (D_2O-bearing) ringwoodite. Time-of-flight (TOF) powder neutron diffraction was carried out at Japan Proton Accelerator Research Complex (J-PARC). Moreover, we also conducted TOF single-crystal Laue diffraction for hydrogenated (H_2O-bearing) ringwoodite at Oak Ridge National Laboratory (ORNL). The latter method is even more suitable to refine the crystal structures because of its much higher resolution in space. It is also applicable even for samples involving light hydrogen (H). We obtained datasets with twice higher spatial resolution than that of our powder neutron datasets. After successful analysis of a single-crystal dataset of hydrogenated ringwoodite, we extended the study into hydrogenated wadsleyite. By applying single-crystal neutron diffraction we obtained datasets with 3 times higher resolution in space [*Purevjav et al.*, 2016] than the previous powder neutron diffraction of deuterated wadsleyite [*Sano-Furukawa et al.*, 2011].

We used a scaled-up Kawai-type cell for the synthesis of hydrous ringwoodite and hydrous wadsleyite, which was installed at Okayama University [*Okuchi et al.*, 2015a; *Shatskiy et al.*, 2011]. During the syntheses experiments, we established a slow-cooling method at very high pressure, which was proved to be effective for growing high-quality and large crystals of deep mantle hydrous minerals [*Okuchi et al.*, 2015a]. The details of this method will be explained in this thesis.

In summary, first, we successfully determined D position and their occupancies in the crystal structure of hydrous ringwoodite [*Purevjav et al.*, 2014]. Then we extended the study into single-crystal neutron diffraction for crystals involving light hydrogen. Hydrogenated ringwoodite was refined with even much higher resolution in space than that of deuterated ringwoodite. We refined the position of light hydrogen and its bonding geometries. We also unambiguously demonstrated the uniqueness of the hydrogen (H^+) site and its occupancy in the crystal structure of wadsleyite. These works were the first application of single-crystal neutron diffraction for the deep-earth hydrous minerals. Based on these results, we will discuss about the difference between hydration mechanisms of wadsleyite and ringwoodite. Finally, we will briefly discuss about their geophysical implications in the relevant mantle conditions.

II. SYNTHESES AND EVALUATIONS OF TRANSITION ZONE MINERALS SUBJECT FOR NEUTRON

II.1. Synthesis strategy of samples for neutron diffraction

In order to obtain good neutron diffraction datasets, we need to prepare chemically homogenous samples of sufficient masses. For that purpose, we used a scaled-up Kawai-type cell for the synthesis experiments, which is installed at Institute for Planetary Materials (IPM) at Okayama University [*Shatskiy et al.*, 2011]. For obtaining good powder neutron diffraction dataset, we need at least an order of magnitude larger mass of the sample than that for powder x-ray diffraction. Moreover, we need three order of magnitude larger volume sample than that for single crystal x-ray diffraction.

Previously, a few powder neutron diffraction studies have been reported for some synthetic hydrous minerals [*Sano-Furukawa et al.*, 2011; *Suzuki et al.*, 2001]. Due to the technical limitations, Suzuki et al [2001] prepared phase G samples with masses of up to 3 mg. Due to such severely-limited amount of the samples, they obtained the neutron diffraction patterns with relatively low signal to background ratios. Later Sano-Furukawa et al [2011] succeeded to prepare deuterated wadsleyite sample of mass of 40 mg, while their sample was not fully deuterated to possible induce a deficient occupancy of D site during the structure refinement. The data of both studies were with limited d-value range.

Single-crystal neutron diffraction for deep mantle hydrous minerals were not conducted yet. In previous studies, researchers synthesized up to almost mm-sized single crystals of wadsleyite and ringwoodite for another purpose [*Shatskiy et al.*, 2009; *Smyth et al.*, 2003]. They used the thermal gradient method for growing the single crystals. By this method, it was enabled to grow large crystals, while the recovered crystals were reported to have inclusions [*Shatskiy et al.*, 2009] and dislocations [*Smyth et al.*, 2003]. By the other previous studies, a slow-cooling method was reported for growing big crystals, while it was applied at pressures only up to 11 GPa [*Loeffert et al.*, 2002; *Shatskiy et al.*, 2010]. For neutron diffraction measurements, chemical inhomogeneity and crystallographic imperfections are not desirable.

Thus here we intend to prepare chemically and crystallographically homogenous samples with sufficient masses, by extending the slow-cooling method toward even higher pressures than 11 GPa. Thus we enabled for growing hydrogenated ringwoodite and hydrogenated wadsleyite single crystals at pressure to 21 GPa.

II.2. Cell assemblies

We newly designed two independent types of cell assemblies for the synthesis experiments, which are named 14/8 and 18/10 cells hereafter (Figure 2.1). The 14/8 cell was used the experiments at pressures up to 21 GPa. The 18/10 cell was used for the experiments at pressures up to 17 GPa. The 14/8 cell consists of octahedral edge length of 14 mm pressure media and 8 mm truncation edge lengths of anvils (TEL). The 18/10 cell consists of octahedral edge length of 18 mm pressure media and 10 mm truncation edge lengths of anvils.

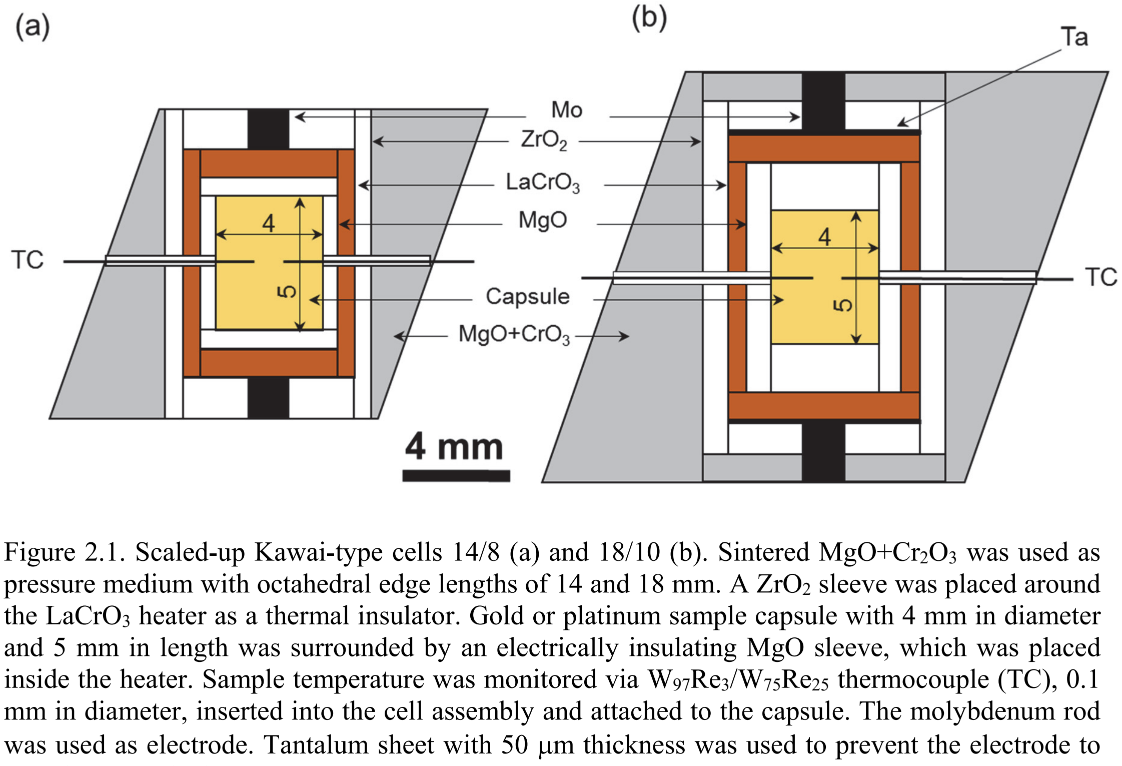

Figure 2.1. Scaled-up Kawai-type cells 14/8 (a) and 18/10 (b). Sintered MgO+Cr_2O_3 was used as pressure medium with octahedral edge lengths of 14 and 18 mm. A ZrO_2 sleeve was placed around the $LaCrO_3$ heater as a thermal insulator. Gold or platinum sample capsule with 4 mm in diameter and 5 mm in length was surrounded by an electrically insulating MgO sleeve, which was placed inside the heater. Sample temperature was monitored via $W_{97}Re_3/W_{75}Re_{25}$ thermocouple (TC), 0.1 mm in diameter, inserted into the cell assembly and attached to the capsule. The molybdenum rod was used as electrode. Tantalum sheet with 50 μm thickness was used to prevent the electrode to intruding into the heater.

All cell parts were prepared by hand using a lathe machine. The parts were baked in oven at 1000 °C for an hour before assembling, which was effective to remove their absorbed water involving light hydrogen. Then the parts were kept in oven at 110 °C until they were assembled, which was for preventing the parts from absorption of water from the air. As a sample container, gold (Au) or platinum (Pt) capsule was used, which are with 4.0 mm in outer diameter and 0.2 mm in thickness and up to 5 mm in length. Pt capsule was used for the experiments with heating temperature up to 1600 °C. Initially tubes of Au and Pt were cut with up to 13 mm in lengths. In order to soften these metals prior to pinch and welding, we baked the Au at 750 °C and Pt at 1000 °C temperatures for an hour in oven, respectively. One side of the tube was pinched into triangle up to 3 mm in length then small pieces were cut from it and welded. The welded side was checked under microscope for observing complete sealing of it. In order to clean inside of the capsule before loading the starting materials, it was soaked into ethanol or acetone then put into an ultrasonic cleaner. After washing the capsule, it was kept at 110 °C in oven in order to dry it. Up to 50 mg of starting materials were then filled into the capsule and then wall of capsule above the starting materials was cleaned well. It was for preventing the leakage of water during the heating from the top side of the capsule. The top side of the capsule was pinched and squeezed using a piston and a jig. The prepared capsule was assembled together with the other cell parts. After assembling the cell, it was combined together with eight pieces of Fujilloy F08 tungsten carbide anvils with 8 mm or 10 mm in TEL with 46 mm or 32 mm in edge lengths (Figure 2.2c). Gaskets were fixed on each anvil's truncated edges using rice paste or cemedine C glue (Figure 2.2b). The gaskets were made of pyrophillite. The gaskets with 4 mm width and 2.83 mm thickness were used for 14/8 cell and those with 5 mm width and 3.77 mm thickness were used for 18/10 cell. Prepared gaskets were baked as same way as the cell parts. Finally assembled cell and anvils were combined together and surrounded by epoxy plate using a double side tape (Figure 2.2d).

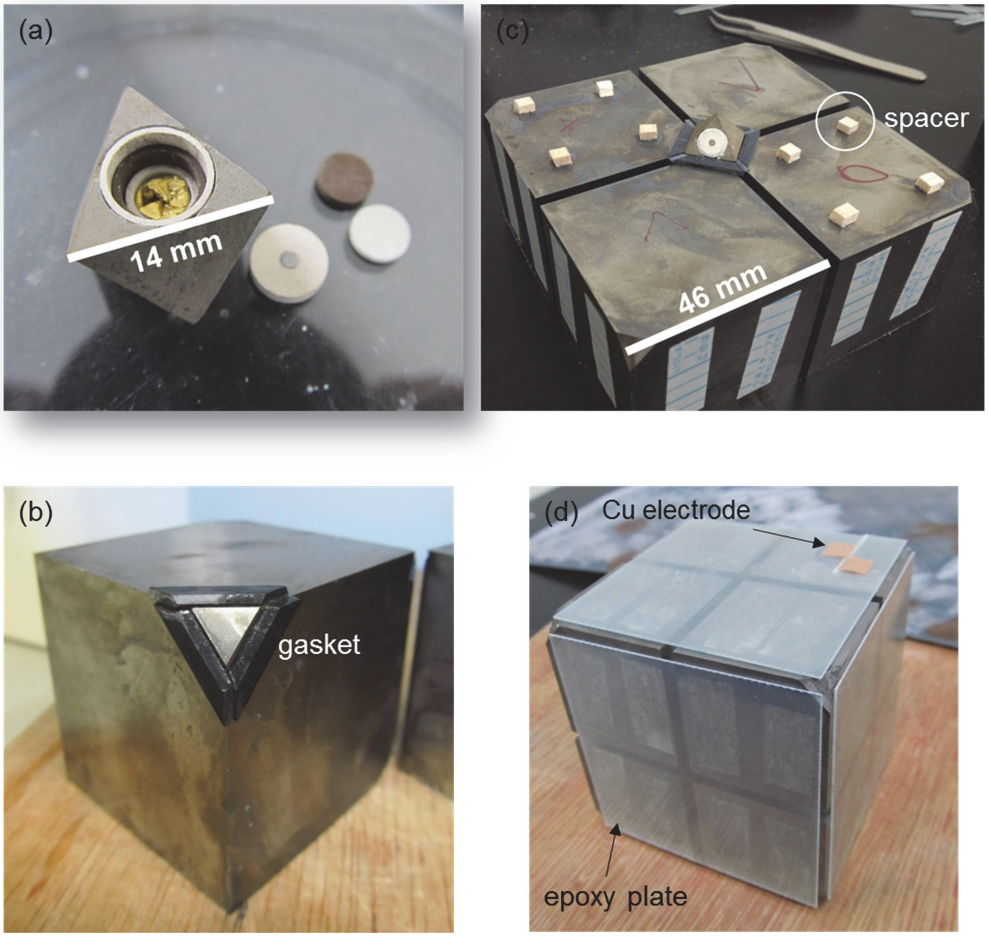

Figure 2.2. Typical a scaled-up Kawai-type cell 14/8.

II.3. Synthesis experiments

The starting material for Fe-bearing ringwoodite was a mixture of San Carlos olivine [$(Mg_{0.91},Fe_{0.09})_2SiO_4$] and D_2O water. The starting material for Fe-free ringwoodite was oxide mixture of MgO, SiO_2 and $Mg(OD)_2$, or a mixture of synthetic forsterite (Fo_{100}) and D_2O water. Single crystals of the San Carlos olivine were crushed to coarse grains and then milled to fine grains using ball milling machine. The SiO_2 glass powder was prepared from a high-purity glass rod, which was crushed and milled as same way as San Carlos olivine. The SiO_2 glass rod was containing less than 20 ppm of OH group, which was commercially available at Shinetsu Sekiei Co. Ltd. For synthesis of $Mg(OD)_2$, dried MgO powder and D_2O water were mixed and heated at 250 °C under autogenic pressure as much as 40 bars for 168 hours in an autoclave, which was heated in vacuum drying oven (DRV320DB, Toyo Seisakusho Kaisha, Ltd). Then the recovered $Mg(OD)_2$ powder was identified by powder x-ray diffraction.

The starting materials for iron-free ringwoodite and wadsleyite were oxide mixture of MgO, SiO_2 and $Mg(OH)_2$. The MgO and $Mg(OH)_2$ reagents were commercially available at Wako Pure Chemical Industries, Ltd, which were with 99.9 % of purity. The MgO had grain size of 0.05 μm and $Mg(OH)_2$ had grain size of 0.07 μm. All starting materials were kept at 110 °C in oven before use. All oxide mixtures were mixed using agate mortar and pestle.

II.3.1. Temperature calibration

We established a power-temperature relation for each cell assembly by conducting several calibration runs in which the temperature of the sample capsule was monitored using a thermocouple (TC). Figure 2.3a and 2.3b show the power-temperature relations for 14/8 and 18/10 cells, respectively. Through a number of experiments, we found that the power-temperature efficiency of both 14/8 and 18/10 cells were fairly reproducible. Thus further experiments were carried out without using TC and the power-temperature calibration was used. We used $y = 1.57x+25$ equation for the 14/8 cell and $y = 1.84x+25$ equation for the 18/10 cell. The reproducibility of the 14/8 cell was ±5 %.

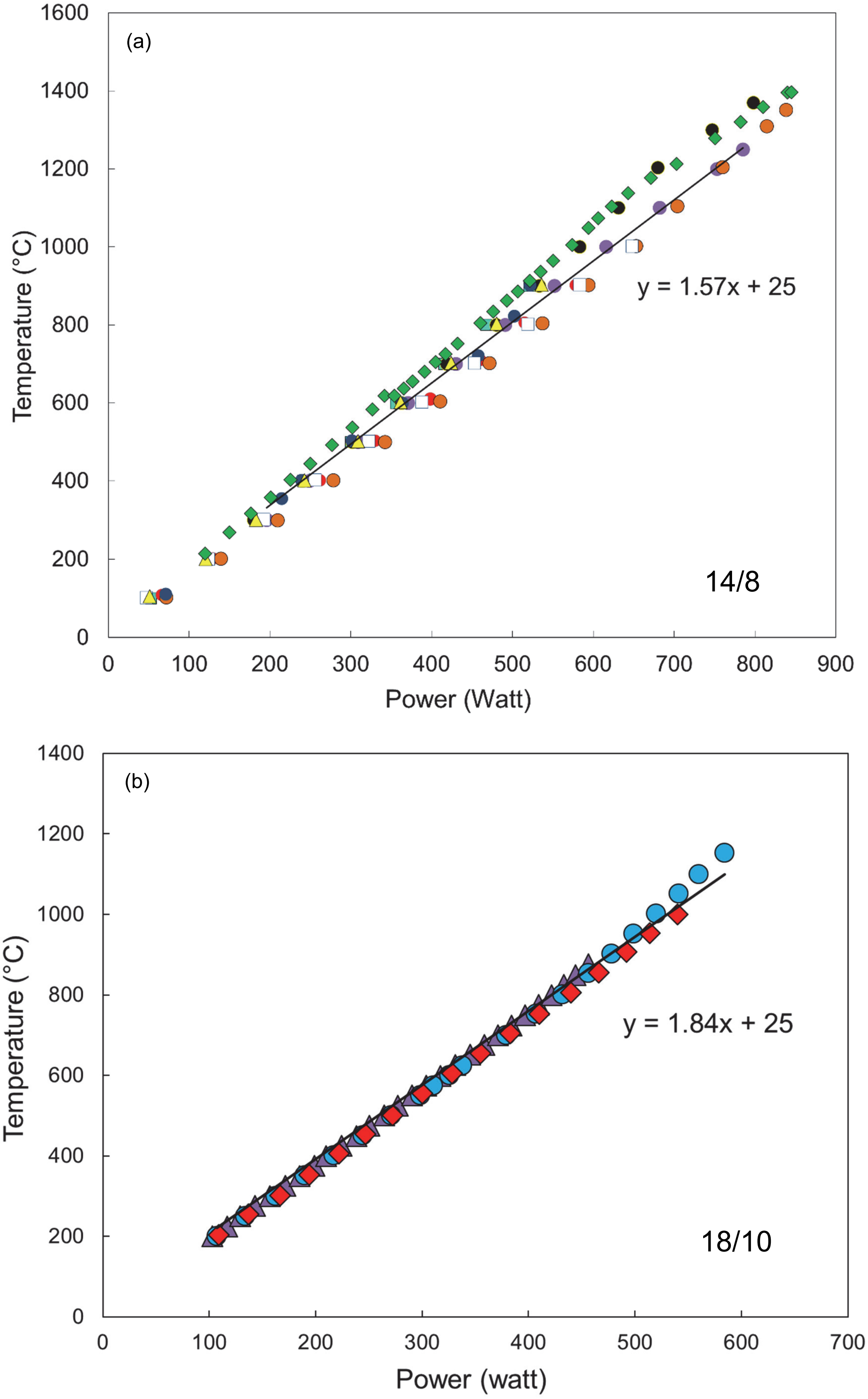

Figure 2.3. Power-temperature relations of 14/8 (a) and 18/10 (b) cells.

II.3.2. Experimental conditions

II.3.2.1. Powder sample synthesis

Here we intended to prepare fully deuterated ringwoodite sample for powder neutron diffraction. It is because D has relatively-large scattering length of neutron than that of H. This scattering length of D is comparable with those of other heavier elements Mg, Fe, Si and O. Also, homogeneity of D concentration is important for the structure refinement of deuterated ringwoodite. Previously, it has been reported that the contamination of H induces occupancy deficiency of D in wadsleyite (*Sano-Furukawa et al.*, 2011). The reason of such deficiency is that negative scattering length of H partly cancells out the positive scattering length of D. It means that the signal from D is smaller than the actual concentration.

Deuterated ringwoodite samples were synthesized using the 14/8 cell (described in the Chapter II.2). Successfully recovered runs are shown in Table 2.1.

Table 2.1. Synthesis conditions and starting materials of each run.

Runs	**P (GPa)**	**T (°C)**	**Duration**	**Starting materials**	**D_2O content (wt.%)**	**Products***
HR5	21	900	3 hrs	SC ol (Fo_{91}) + D_2O	6	Rw
HR8	21	900	3 hrs	SC ol (Fo_{91}) + D_2O	6	Rw
HR11	21	900	30 min	SC ol (Fo_{91}) + D_2O	7	Rw +SuB
HR12	21	1350±5	2.5 hrs	$MgO+SiO_2+ Mg(OD)_2$	11	Rw+Aki
HR13	17	1200	30 min	SC ol (Fo_{91}) + D_2O	8	Rw+E
HR14	21	1330±20	1.5 hrs	$MgO+SiO_2+ Mg(OD)_2$	5	Rw+Aki
HR17	21	1350±20	1 hr	$MgO+SiO_2$(10% reduced) $+Mg(OD)_2$	11	Aki+SuB
HR18	21	1250±10	30 min	$MgO+SiO_2+ Mg(OD)_2$	5	Aki+SuB+Sti
HR19	17	1000±30	30 min	SC ol (Fo_{91}) + D_2O	5	SuB+ E
HR20	21	1350±4	45 min	$Fo_{100}+D_2O$	11	Sub+Sti+Rw
HR22	19	900	10 min	SC ol (Fo_{91}) + D_2O	5	Rw+SuB
HR23	19	1300±1	5 min	SC ol (Fo_{91}) + D_2O	5	Almost pure Rw
HR24	19	1300±1	5 min	SC ol (Fo_{91}) + D_2O	5	Almost pure Rw
HR25	19	1300±1	5 min	SC ol (Fo_{91}) + D_2O	5	Almost pure Rw

*Rw – Ringwoodite; SuB – Superhydrous phase B; Aki – Akimotite; E – Phase E; Sti – Stishovite

We recovered dry ringwoodite samples at lower temperature, longer duration and lower water content condition. At higher temperature, longer duration and higher water content, we recovered ringwoodite with additional hydrous phases, while almost pure ringwoodite was recovered at higher temperature, shorter heating duration and lower water content condition.

II.3.2.2. Single crystal sample synthesis

The both 14/8 and 18/10 cells were used for synthesis of hydrogenated ringwoodite and wadsleyite single crystals. Experiments were carried out with by far longer heating duration than that for powder sample synthesis. The most successfully recovered runs details are shown in Table 2.2. and Table 2.3. The pressures were generated by applying load [*Frost et al.*, 2004; *Shatskiy et al.*, 2011]. Once target pressure was attained the capsule was started to be heated up to desired temperatures. After reaching the desired temperature, we started to reduce the temperature very slowly taking for 3 to 24 hours. Example profiles are shown in Figure 2.4 and Figure 2.5. Previously, this slow-cooling method were reported as effective way to grow single crystals even at high pressures up to 11 GPa [*Loeffert et al.*, 2002; *Shatskiy et al.*, 2010], while in this study we applied it at twice higher pressures up to 21 GPa. Through these synthesis experiments, we established that the slow-cooling method is also effective to grow single crystals of deep mantle minerals of high quality [*Okuchi et al.*, 2015a]. The quality of recovered crystals was examined using various methods, which is shown in Chapter II.4.

Table 2.2. Synthesis conditions of hydrogenated ringwoodite.

Runs	**P (GPa)**	**T (°C)**	**Duration (hours)**	**Starting materials**	**Products***	**Crystal size (μm)**	**Lattice constant (Å)**
HR37	21	1400→1200	10	$MgO+Mg(OH)_2+SiO_2$ with 10 wt.% H_2O	Rw+Aki	700	8.0795(3)
HR38	21	1400→1240	10	$MgO+Mg(OH)_2+SiO_2$ with 15 wt.% H_2O	Rw+SuB	600	8.0823(3)
HR42	21	1400→1340	3	$Fo_{100}+H_2O$ (10 wt.%)	Rw+SuB	600	8.0815(3)

*Rw-ringwoodite; Aki-Akimotoite; SuB-superhydrous phase B

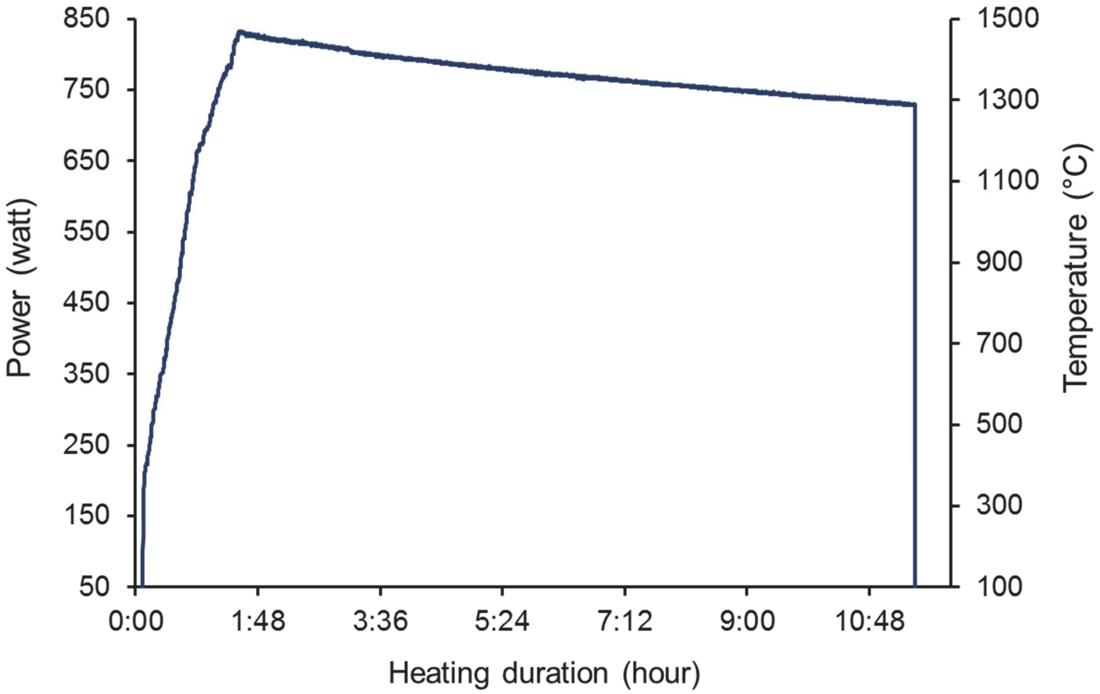

Figure 2.4. Typical heating profile for the synthesis of hydrogenated ringwoodite single crystals (HR38).

Table 2.3. Synthesis conditions of hydrogenated wadsleyite.

Runs	Cell type	T (°C)	Duration (hours)	H_2O content (wt.%)	Products*	Crystal size (μm)
HW6	14/8	1350→1300	6	10	Wd+Cen	400
HW7	14/8	1400→1300	24	10	Wd+Cen	500
HW8	14/8	1400→1360	6	15	Wd+Cen	800
HW10	14/8	1400→1360	6	18	Wd+E	700
HW11	18/10	1500→1450#	6	18	Wd+Cen	600
HW12	18/10	1500→1420#	10	18	Wd+Cen+L	500
HW13	18/10	1500→1440#	6	15	Wd+Cen	400
HW14	18/10	1400→1360	6	15	Wd+Cen	500
HW18	14/8	1390→1320	10	15	Wd+Cen+L	1100
HW19	18/10	1600→1500#	6	15	Wd+Cen	500

#Pt capsules were used for a sample container
*Wd – wadsleyite; E – phase E; Cen – clinoenstatite; L – liquid

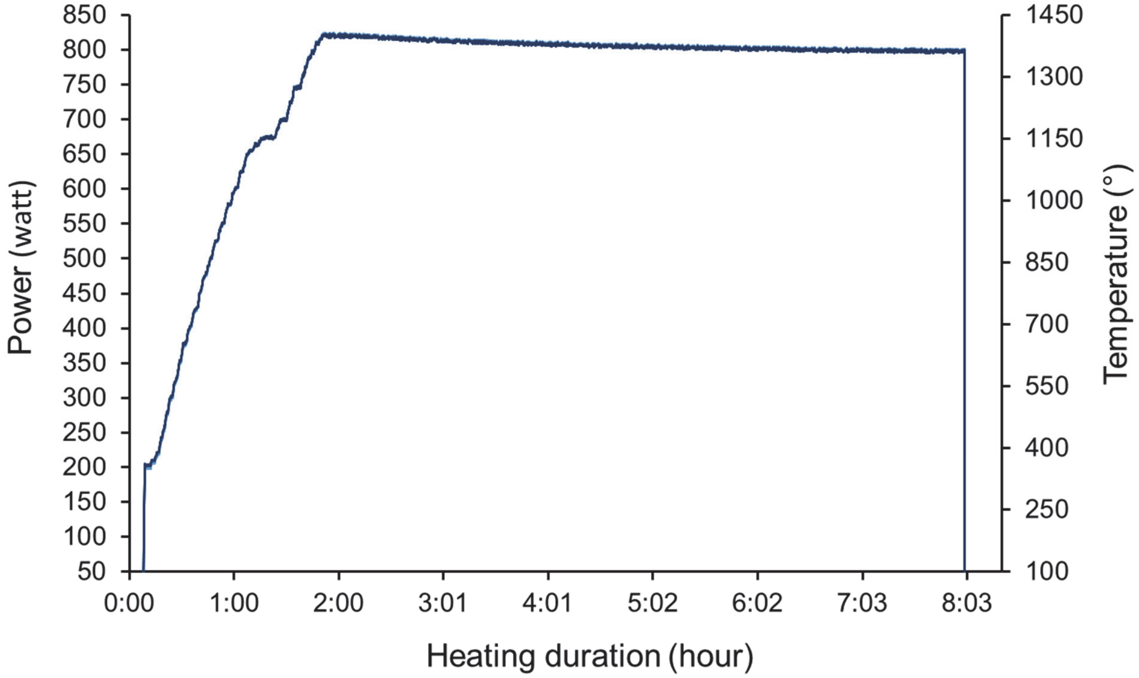

Figure 2.5. Typical heating profile for the synthesis of hydrogenated wadsleyite single crystals (HW8).

II.4. Evaluation of recovered samples

All the recovered run products were separately measured by microfocus x-ray diffractometer (Rigaku RINT RAPID II-CMF) for initial phase identification. We typically recovered 50 mg of sample from powder synthesis experiments.

II.4.1. Powder x-ray diffraction

Each recovered sample was separately measured by powder x-ray diffractometer (PXRD) (Rigaku SmartLab) in order to determine their lattice constants and possible contaminations of additional phases. We picked up several polycrystal aggregates from several areas of each recovered capsule of powder synthesis experiment. Then the aggregates were grinded together into fine grain using agate mortar in dry condition. In contrast, we selected a few single crystals from each recovered capsule of single crystal synthesis experiments and obtained their microfocus x-ray patterns. The crystals were grinded as same way as the polycrystalline samples. Then each grinded sample was independently measured by PXRD. The samples were measured with Cu$K\alpha_1$ radiation operated at 40 kV and 30 mA. Each sample was loaded on the top of a single crystal Si plate then flattened using glass slide and measured at room temperature. The plate used as a sample holder and it has very low background. We can measure small amount of samples using this plate. The diffraction patterns were obtained by the step scanning method with step size of 0.0052° and scan speed of 0.1°/min in distinct 2θ ranges. The 2θ angles were calibrated by the silicon powder standard (NIST640d) as an external standard, and their lattice constants were refined through least-squares fitting of peak positions by using the UnitCell software [*Holland and Redfern*, 1997].

II.4.1.1. Deuterated ringwoodite

Successfully recovered each charge of deuterated ringwoodite was separately measured by PXRD. The diffraction patterns were obtained with a 2θ range of 10–140°. By this step HR5

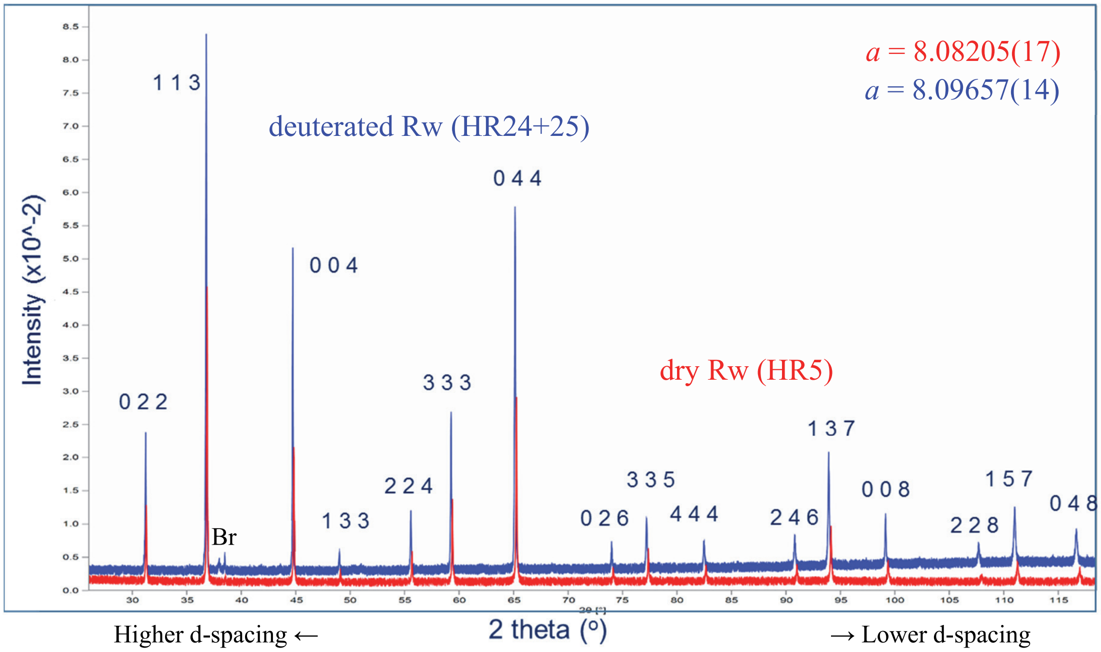

Figure 2.6. Diffraction patterns of dry (HR5) and deuterated ringwoodite (Rw) (HR 24+25). Br is brucite.

and HR8 samples were proved to be the single phase of dry ringwoodite. Thus we chose HR5 as the reference sample, which has the lattice constant of a_0 = 8.08205±17 Å and V_0 = 527.916±19 Å^3. Run products of HR23, 24 and 25 were proved to be made of almost-pure ringwoodite phase with trace amount of brucite. The lattice constants of HR24 and HR25 were a = 8.09687±15 Å and a = 8.09544±15 Å respectively, which were almost identical. Thus these two batches were mixed together to prepare enough mass of the sample for neutron diffraction. The mixed sample of HR24+25 was also measured by PXRD to give the averaged lattice constant of a = 8.09657±14 Å and V = 530.766±16 Å^3. We compared diffraction patterns of HR5 and HR24+25 and found that the reflections of HR24+25 were shifted into lower 2θ range compared with those of HR5 (Figure 2.6). Such shifting must be influenced by the deuteration of the structure, which results the expansion of unit cell. Thus this lattice expansion must be increased by the deuteration because the dry (HR5) and the deuterated (HR24+25) samples have the same Fo_{91} composition.

From the lattice constant difference, we estimated the D_2O content of HR24+25 mixed sample. We assumed that D_2O and H_2O has identical effect on the unit cell expansion. We used empirically reported lattice volume and water concentration relation [*Ye et al.*, 2012]. The HR24+25 sample was found to be containing 0.34 D per formula unit (pfu), which corresponds 2.4 wt.% of D_2O.

II.4.1.2. Hydrogenated ringwoodite

Hydrogenated ringwoodite single crystals were synthesized together with additional hydrous or anhydrous phases. We selected the ringwoodite crystals from each run product by referring their microfocused x-ray patterns. Then the selected crystals were measured by PXRD. The obtained patterns indicated the single phase of ringwoodite. The diffraction patterns were obtained with a 2θ range of 10–130°. From each refined lattice constant, we estimated the H_2O concentration involved in the corresponding product crystals. The estimated lattice constant of each samples is shown in Table 2.2 (Chapter II.3.2.2). We referred the previously reported lattice constant of dry ringwoodite (a = 8.0649±1 Å) [*Sasaki et al.*, 1982] and found that all the recovered run products had significantly larger lattice constants. The lattice constant of HR38 was largest among the recovered runs. If we refer the empirically-reported relation between lattice volume and water concentration by Ye et al [2012], HR38 should contains more than 2 wt.% of water. Thus HR38 crystals with a moderately-large size of 600 μm were chosen for the subject for single-crystal neutron diffraction.

II.4.1.3. Hydrogenated wadsleyite

Wadsleyite crystals were synthesized and recovered together with hydrous and anhydrous additional phases. We picked up few tens of wadsleyite crystals from each recovered capsule. Sample preparation of hydrogenated wadsleyite follows the same way as for hydrogenated ringwoodite. The diffraction patterns were obtained by the step scanning method with a 2θ range of 10°–140°. Obtained diffraction patterns of each recovered run crystals were single phase of wadsleyite and their lattice constants were determined independently. Then we calculated their *b/a* axial ratio, which was used for determining their H_2O content. Previously, it was reported that empirical relationship between *b/a* axial ratio and H_2O concentrations in wadsleyite [*Jacobsen et al.*, 2005] (Figure 2.7). Determined lattice constants and corresponding water concentrations are tabulated in Table 2.4. From this analysis, we chosen wadsleyite crystals from HW8 for possible candidate for neutron diffraction, which are evaluated by further analysis.

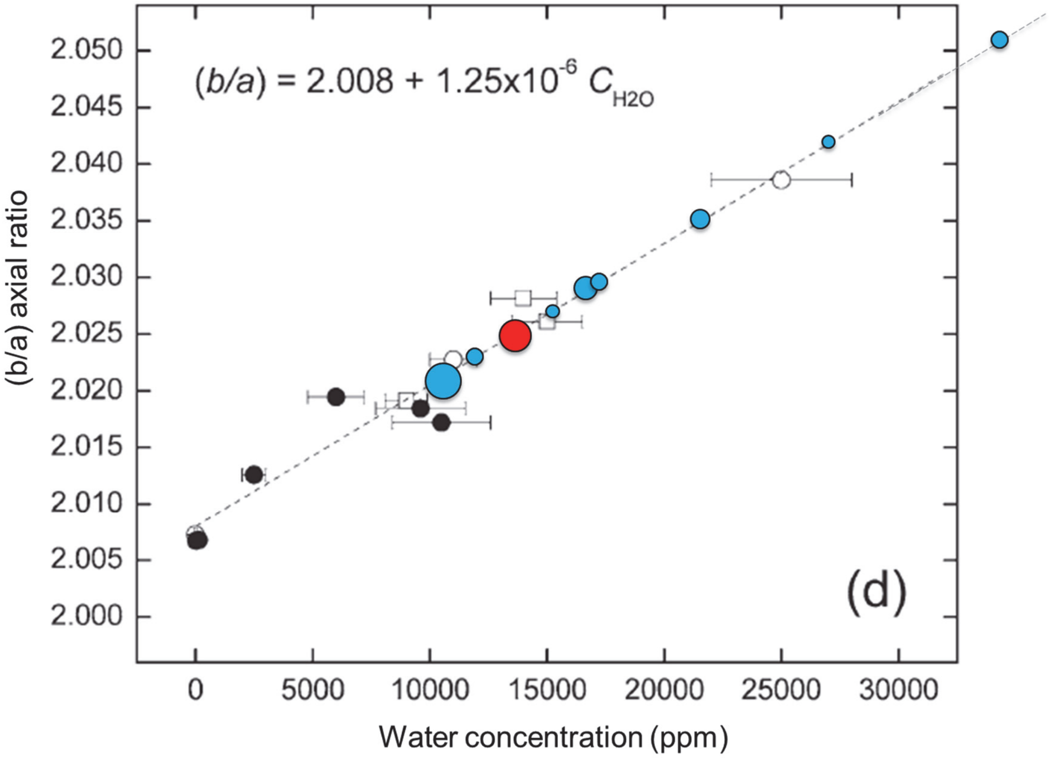

Figure 2.7. The *b/a* axial ratio against water concentrations [*Jacobsen et al.*, 2005]. Water concentrations were determined by infrared spectroscopy and SIMS and the lattice constants were determined by x-ray diffraction. Blue and red circles are our synthesized wadsleyite, which are plotted based on their *b/a* axial ratio. The size of circles corresponds to the biggest size of recovered crystals from each run. The smallest circle corresponds 400 μm and biggest circle corresponds 1100 μm size of crystals. The red circle is crystal recovered from HW8 run.

Table 2.4. Lattice constants of recovered wadsleyite crystals.

Runs	**Lattice constants (Å)**			**Volume ($Å^3$)**	***b/a* ratio**	**H_2O* (wt.%)**
	a	***b***	***c***			
HW6	5.6834(4)	11.521(2)	8.2534(7)	540.45(2)	2.027	1.6
HW7	5.6870(4)	11.513(2)	8.2568(8)	540.60(9)	2.024	1.3
HW8	5.6865(4)	11.515(2)	8.2545(7)	540.52(5)	2.025	1.3
HW10	5.6823(6)	11.527(1)	8.250(1)	540.38(8)	2.029	1.7
HW11	5.6738(6)	11.547(2)	8.2438(7)	540.09(8)	2.035	2.1
HW12	5.6852(4)	11.502(1)	8.2545(7)	539.30(8)	2.023	1.2
HW13	5.6717(6)	11.581(2)	8.2460(7)	541.29(9)	2.042	2.7
HW14	5.6618(9)	11.615(3)	8.2399(7)	541.9(1)	2.051	3.4
HW18	5.6882(6)	11.497(2)	8.255(8)	539.89(9)	2.021	1
HW19	5.6812(6)	11.532(1)	8.2493(7)	540.48(7)	2.03	1.7

*estimated water concentration from b/a ratio [*Jacobsen et al.*, 2005]

II.4.2. Raman spectroscopy

We obtained a few Raman spectra for detection of OD and OH stretching vibrations in the recovered deuterated ringwoodite samples. We took several aggregates from the mixed sample of HR24+25 and embedded into epoxy then polished. The polished aggregates were measured by micro-Raman spectroscopy. We observed intense OD vibration at 2686 cm^{-1} (Figure 2.8), which was corresponded to vibration wavenumber of brucite [$Mg(OD)_2$] [*Okuchi et al.*, 2013]. We did not observe any OH vibration in this spectrum. It means that the all run charges had negligible contamination of OH, which indicated that the coexisting ringwoodite must have also negligible contamination of OH. The origin of this deuterated brucite will be discussed later.

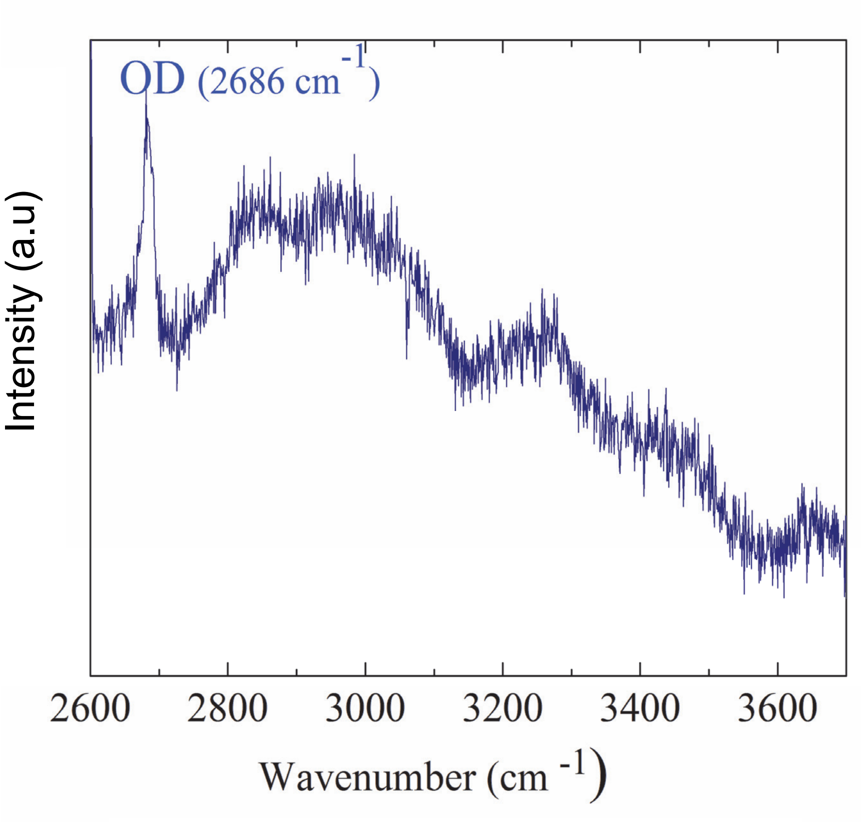

Figure 2.8. A representative Raman spectrum of HR24+25.

II.4.3. Infrared spectroscopy

We measured single crystals of hydrogenated wadsleyite from HW8 run. Three crystals of wadsleyite with up to 300 μm in size were embedded into orthodontic resin (Caulk ®) then polished. We measured the doubly polished crystals by micro-Fourier transform infrared (FTIR) spectrometer (Jasco FTIR6200-IRT7000). This instrument is equipped with 10x Cassegrain optics, a Ge-coated KBr beam splitter, a MCT (mercury-cadmium-telluride) detector cooled by liquid nitrogen and a ceramic light source. IR beam was focused on crystals with 30x30 μm spot size by adjusting aperture. KBr crystal was used as a sample base, which does not absorb the beam. Each measurement was done using unpolarized IR beam with 1024 scans accumulated for each spectrum with wavenumber resolution of 4 cm^{-1}. We measured several spectra from each crystal. Obtained spectra for each crystal were identical each other.

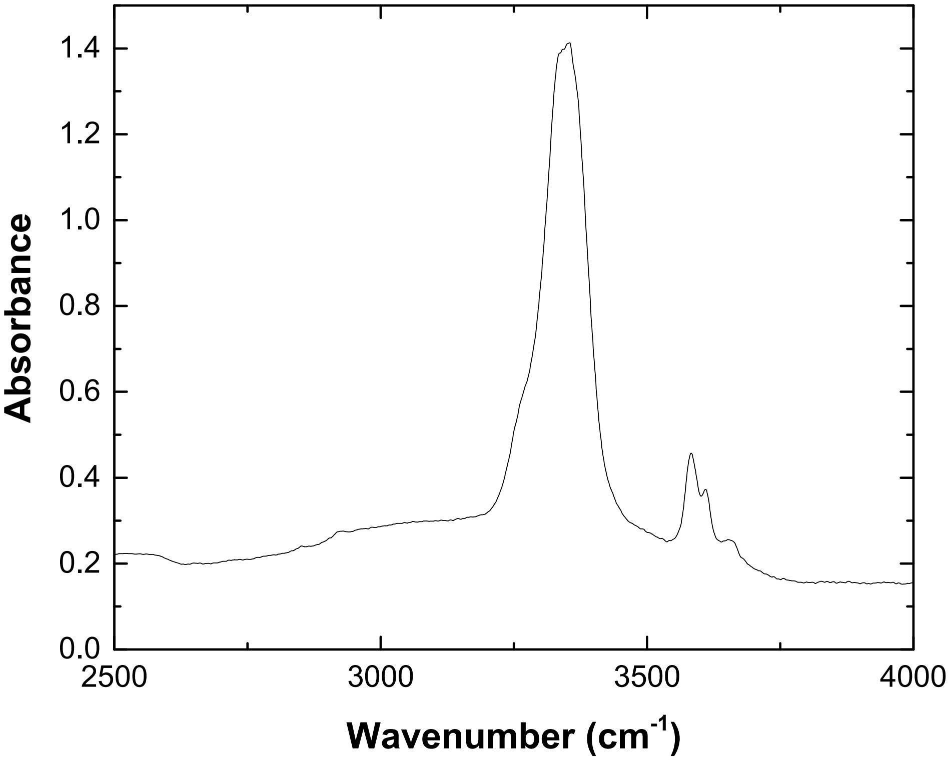

Figure 2.9. A representative IR spectrum of hydrous wadsleyite. The spectrum was obtained from the crystal with 30 μm in thickness. The thickness of crystal was measured with a Mitsutoyo Litematic 318 displacement gauge with an accuracy of ±2 μm.

Therefore, water concentration was homogenous in each crystal. A representative spectrum is shown in Figure 2.10. The obtained shape of spectra resembled the typical spectrum of hydrous wadsleyite, which were reported previously [*Bolfan-Casanova et al.*, 2000; *Jacobsen et al.*, 2005].

II.4.4. Electron probe analysis

Chemical homogeneity of the mixed sample HR24+25 was analyzed by electron probe microanalyzer (EPMA; JEOL JXA-8800). We embedded five aggregates from the mixed sample HR24+25 into epoxy resin and polished in dry condition. Then the polished sample was coated with carbon and measured by EPMA. Prior to the measurement, we also measured dry San Carlos olivine as the additional standard. The electron beam was with 15 kV in acceleration voltage, and 8–12 nA in current. The exposure time of each measurement was 20 seconds. We analyzed 11 points from those five aggregates. The average chemical composition of HR24+25 was $Fo_{91.1\pm0.3}$, the average ratio of (Mg+Fe)/Si was 1.92±0.03, and the total weight of major elements was 98.3±1.0 wt.% (all uncertainties are 1σ). The polished samples were also observed by field-emission scanning electron microscope (FE-SEM; JEOL JSM-7001F) in order to observe possible chemical zoning. We found that the deuterated ringwoodite grains were all less than 50 μm in size and don't have any visible chemical zoning (Figure 2.10a).

Crystallinity of hydrogenated wadsleyite crystals was observed by FE-SEM. Two crystals of hydrogenated wadsleyite with more than 500 μm were observed and sample preparation followed same way as the deuterated ringwoodite sample. The polished crystals also were coated by carbon. We obtained backscattered electron images of these two crystals and we found that the hydrogenated wadsleyite crystals were free from inclusion and twinning. Also these crystals had no visible chemical zoning (Figure 2.10b).

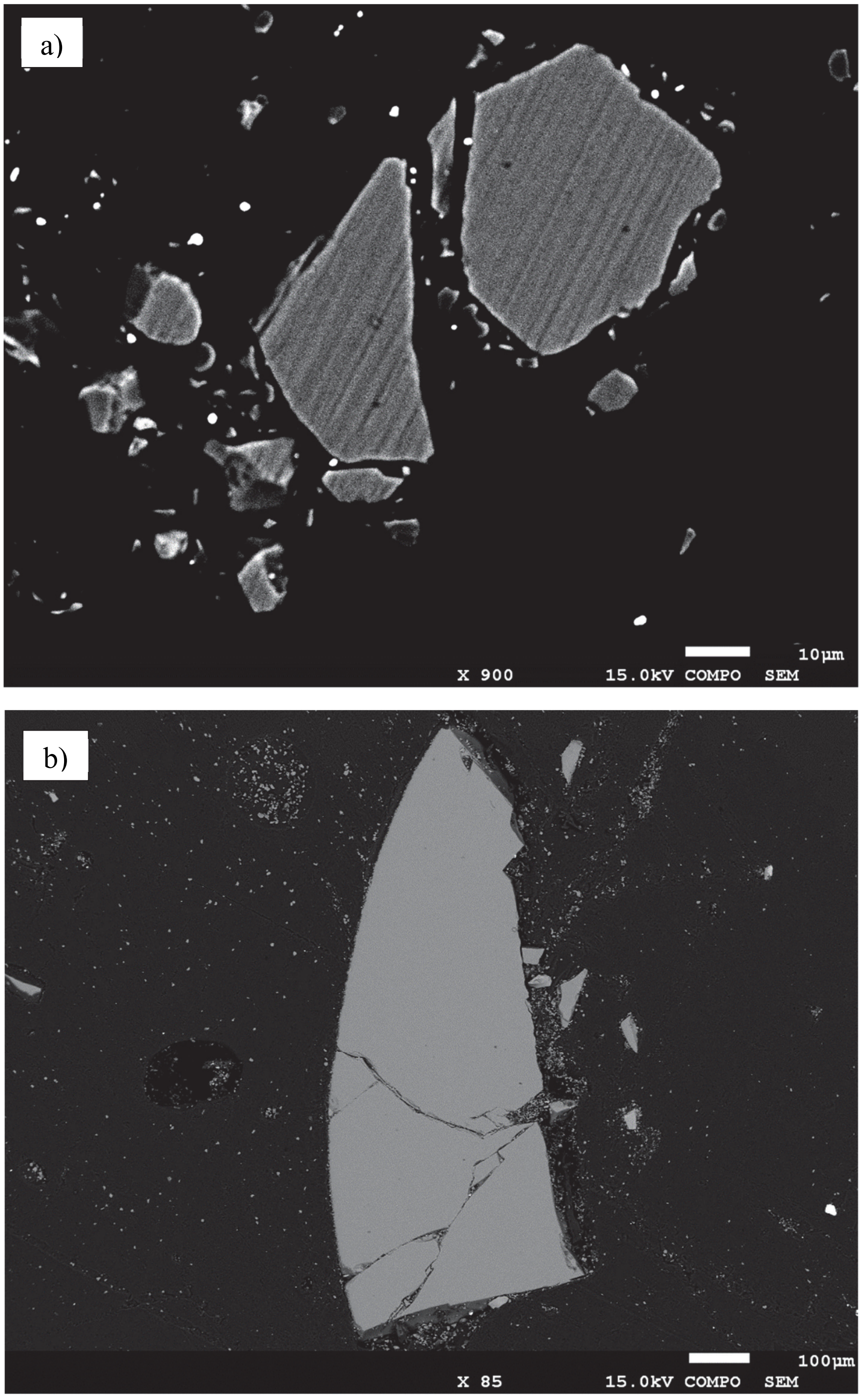

Figure 2.10. Backscattered images of polished samples (a) deuterated ringwoodite and (b) hydrogenated wadsleyite.

II.4.5. Precession x-ray photography

The precession x-ray photography was applied for observing possible imperfections of crystals such as twinning and inclusion. A precession camera (Rigaku 1533A2) was used for two hydrogenated wadsleyite crystals. Crystals were exposed using Mo$K\alpha_{1,2}$ radiation operated at 30 kV and 30 mA for 20 minutes.

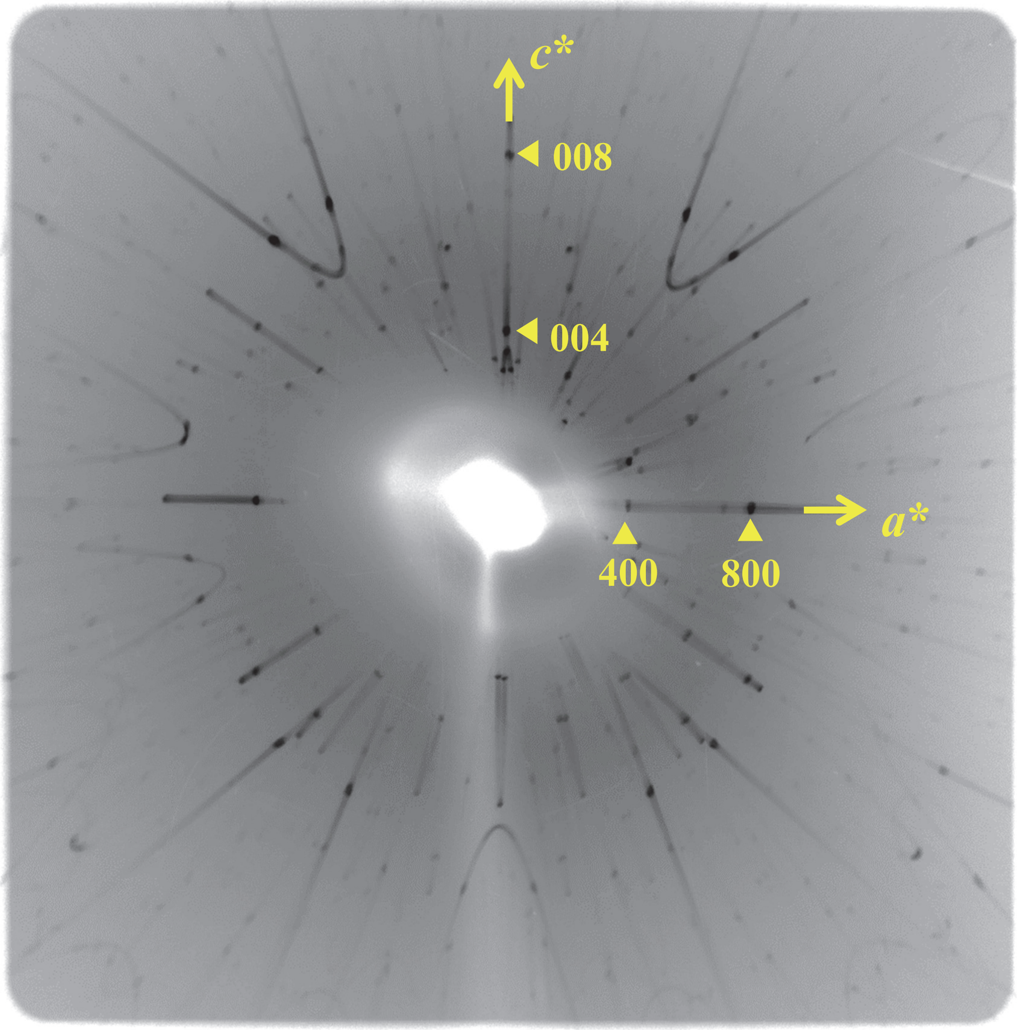

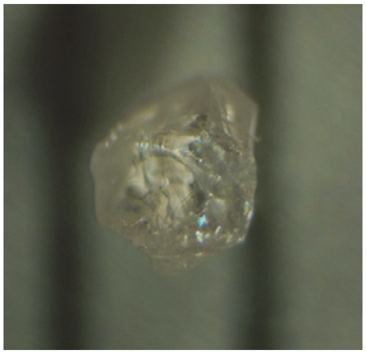

Figure 2.11. A precession photography of the measured hydrous wadsleyite (HW8) at the single-crystal neutron diffraction. The numbers denote Miller indices of diffraction spots indicated by arrows.

Two biggest crystals from HW8 were fixed on the fiber glass with size of 1 mm in diameter using colorless nail color. From this observation we confirmed that the crystals from HW8 run are free from any inclusion and twinning. Thus the one of these two was chosen for the neutron diffraction (Figure 2.11).

III. NEUTRON DIFFRACTION

III.1. Time-of-flight method

Neutron is an elementary particle consisting atomic nuclei together with protons. Neutron has zero charge and interacts only with the nucleus of atoms, while x-ray rather interacts with electrons. Neutron scattering lengths of light atoms can be similar magnitude as those of heavy atoms, while x-ray scattering length increases monotonically with increasing atomic number. Therefore, as for hydrogen, scattering length by neutron is much larger than that of x-ray. Also neutron scattering lengths of H and D are significantly different each other, including their signs.

There are two types of neutron sources, which are reactor and spallation sources.

1. In reactor sources, neutrons are produced by fission chain reaction of very heavy nuclei. Figure 3.1a shows a schematic of the fission process. When a neutron is absorbed into a heavy nucleus such as ^{235}U, a large amount of energy is transferred into the system. Then excited unstable nucleus (^{236}U) fissions into stable nucleus and free neutrons. The liberated neutron is again absorbed into another heavy nucleus and so on. This reaction continuously repeats and produces a large number of neutrons, while their production time and kinetic energy are variable. In that case all the neutrons can't be used simultaneously for diffraction and they must be monochromized before use. Through this procedure monochromatic wavelength of neutron is selected (λ=constant). Neutron diffraction satisfies the Bragg's law ($\lambda = 2d\sin\theta$) under this constant wavelength.
2. In spallation sources, a large number of accelerated protons are injected to moderately heavy nuclei like mercury (Figure 3.1b). Then target nuclei is spalled to generate a large number of neutrons simultaneously. The advantage of spallation sources is therefore that they have definable injection time of protons and production time of neutrons. Then traveling times of produced neutrons are well defined if their arrival times are known. This method is called time-of-flight (TOF). Wavelengths of neutrons are obtained from

the equation $\lambda = \frac{ht}{mL}$, where h is Planck's constant (6.626 x 10^{-34} Js), m is the neutron mass (1.675 x 10^{-27} kg), t is TOF and L is total path length. Thus using these known wavelengths of neutrons, we can obtain the reflections with variable d-spacing simultaneously. Here we used the TOF method at Material and Life Science Experimental Facility (MLF) in Japan Proton Accelerator Research Complex (J-PARC) and Spallation Neutron Source in Oak Ridge National Laboratory (ORNL).

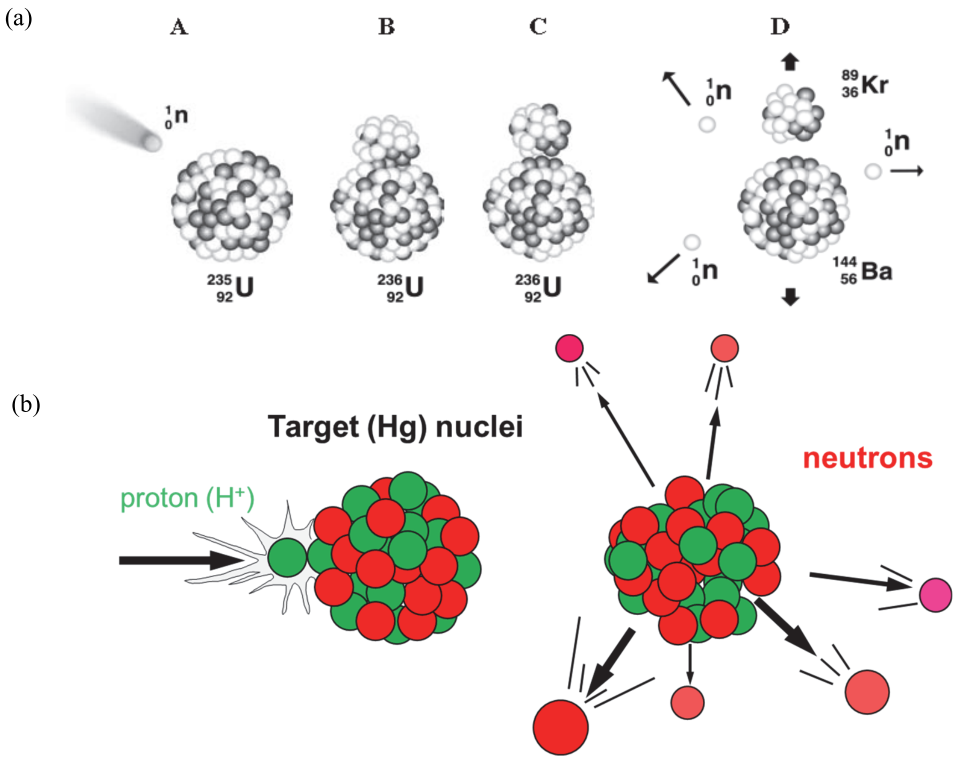

Figure 3.1. (a) Neutron generation in Reactor sources, modified after [*Vogel and Priesmeyer*, 2006]. (b) Neutron generation in Spallation sources.

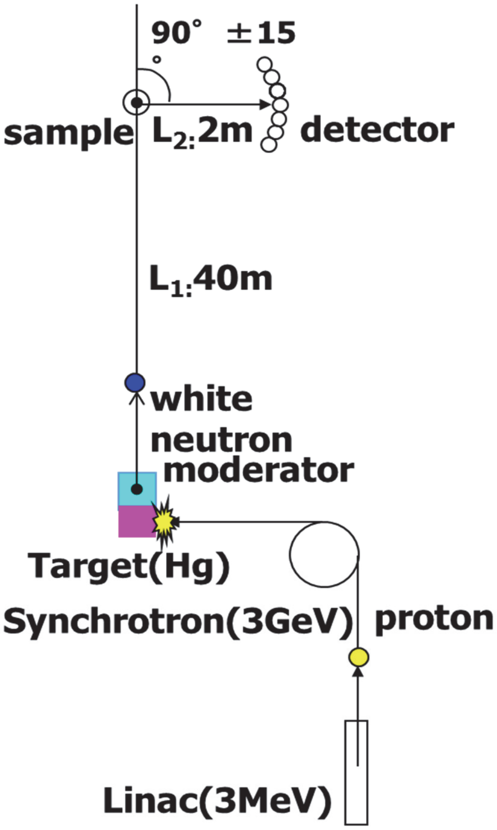

Figure 3.2. Schematic view of time of flight method in case of TAKUMI at J-PARC.

III.2. Data collection procedures

III.2.1. Powder neutron diffraction measurement

Powder diffraction measurement was conducted at Engineering Materials Diffractometer "TAKUMI" (Beamline 19) were installed at Materials and Life Science Experimental Facility at J-PARC [*Harjo et al.*, 2006]. TAKUMI has two detector banks cover 90±15° horizontal and ±16° vertical scattering angles from the sample position. It provides a moderately-high resolution of $\Delta d/d \sim 0.3$ % in its medium-resolution mode (Figure 3.3). This mode provides not only high d-value resolution along with symmetric peak shapes, but also moderate neutron beam intensity. Radial collimators with 5 mm in gauge volume were used to shield spurious neutrons from air or other scattering. The deuterated mixed sample HR24+25 with mass of 66 mg was loosely filled into a cylindrical shaped sample container, which has size of 3.0 mm outer and 2.4 mm inner diameter made of hardened Ti-Zr null alloy (Figure 3.4). This sample container was especially designed for this measurement. Ti-Zr alloy has no coherent scattering of neutron and it means that it is almost transparent for neuron. It has composition of Ti (68 atom %) and Zr (32 atom %). It means that Ti-Zr cell does not degrade neutron diffraction patterns of the samples [*Okuchi et al.*, 2015b]. The sample position was adjusted to the center of the neutron beam using telescopes. This procedure was dedicated to match the center of sample to the center of neutron beam in 50 μm accuracy. The sample was exposed for the beam for 8 hours at 300 kW power. We successfully obtained the pattern with the sufficient ratio of signal to background (Figure 3.5). The obtained raw diffraction pattern was intensity-normalized using a profile of vanadium pellet of comparable dimension to the sample, which was separately measured using the same neutron optics.

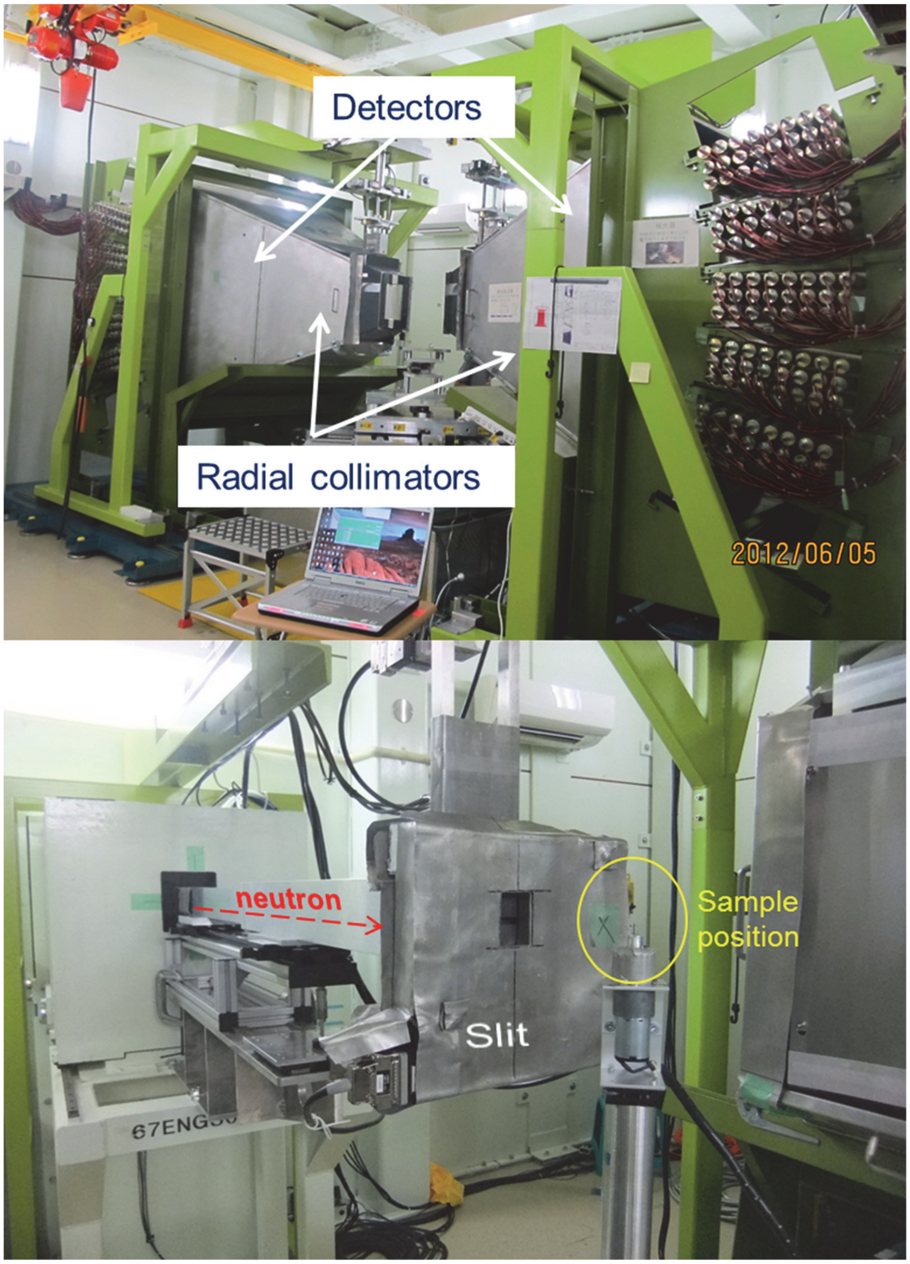

Figure 3.3. Engineering diffractometer TAKUMI.

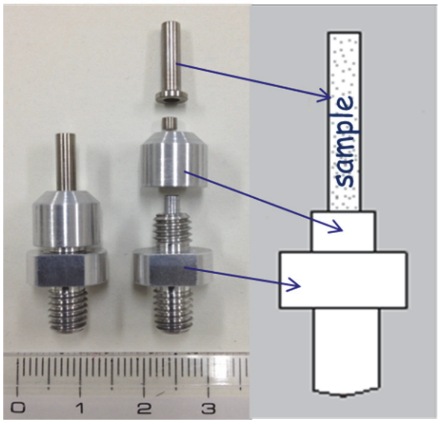

Figure 3.4. Ti-Zr sample container

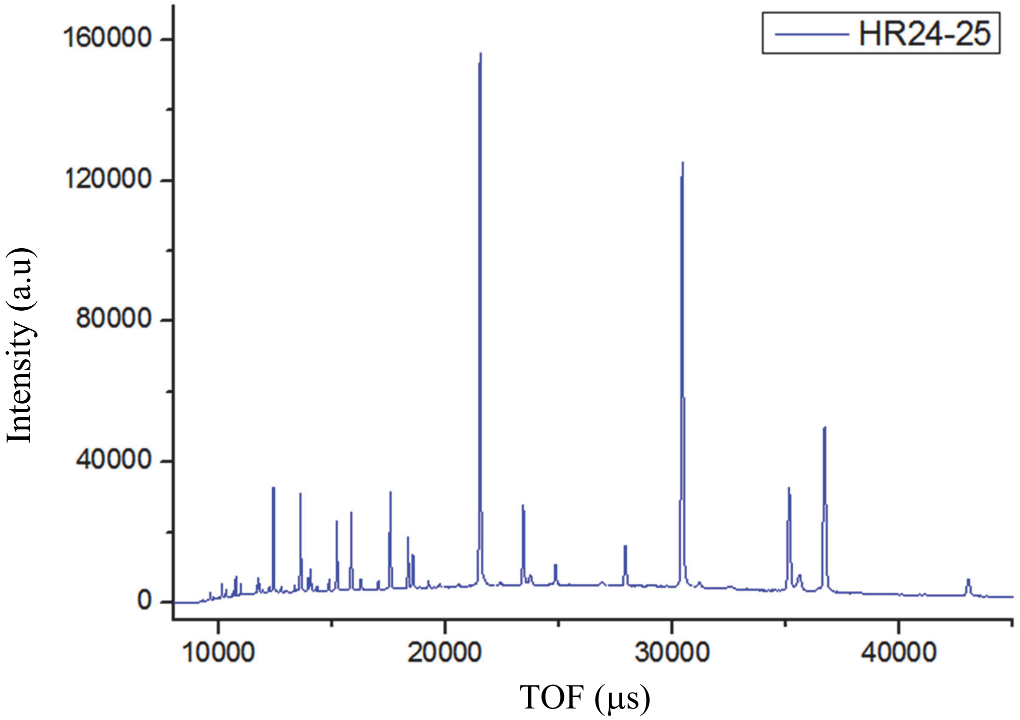

Figure 3.5. Obtained raw pattern of mixed sample HR24+25 without any background subtraction.

III.2.2. Single-crystal neutron diffraction measurements

Single-crystal diffraction measurement was carried out at TOF Laue single-crystal diffractometer TOPAZ (Beamline 12) [*Schultz et al.*, 2014] installed at SNS, ORNL. TOPAZ has 13 detectors covering scattering angles of about 20–160° 2θ, covering 1.2 sr in an almost spherical arrangement around the sample. Each detector is with active areas of 15 x 15 cm^2 (Figure 3.6). The moderator to sample fight path is 18 m and the sample to detector flight distance vary in the range 39 – 46 cm.

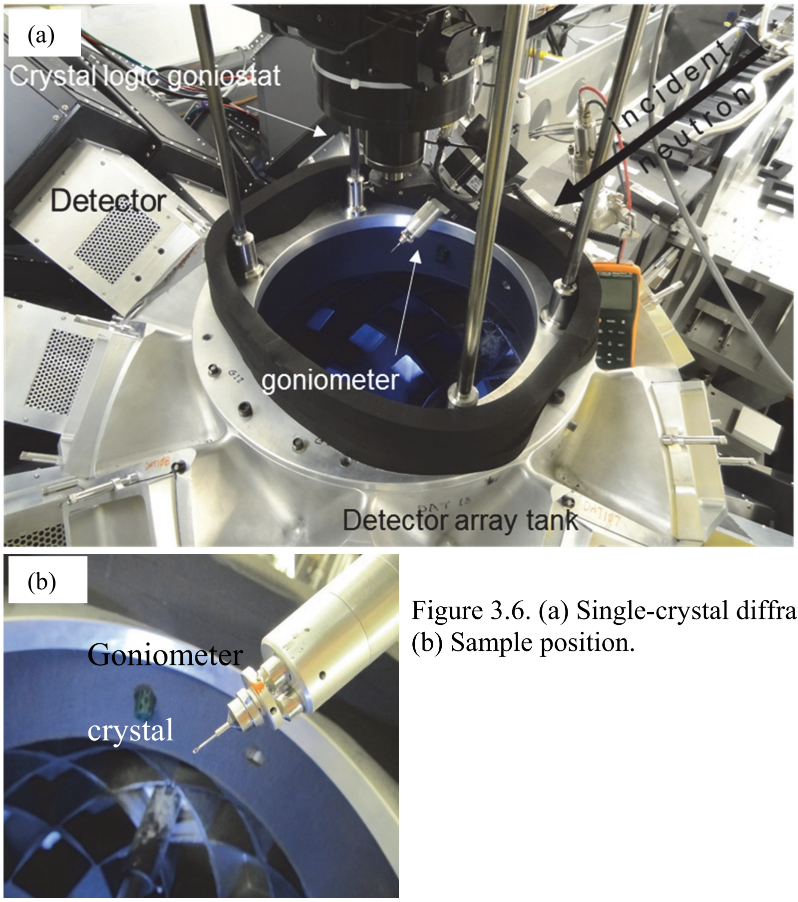

Figure 3.6. (a) Single-crystal diffractometer TOPAZ. (b) Sample position.

The hydrogenated ringwoodite crystal with 600 μm in size (HR38) was mounted on a loop with 1 mm in diameter (Figure 3.7a). The hydrogenated wadsleyite crystal with 800 μm in size was mounted on a 500 μm diameter pin-base polyimide tube using a small amount of epoxy resin under a microscope setup (Figure 3.7b and c). The both crystals were separately measured at 100 K temperature for two to three days. Also hydrogenated wadsleyite was measured at 295 K. The low temperature environment was attained using a nitrogen cold gas flow. The low temperature was effective to reduce Debye-Waller factors of each atom and to obtain more intense reflections. The most effective data collection procedure for each crystal was calculated and optimized using *CrystalPlan* software [*Zikovsky et al.*, 2011]. We verified that neutron intensities of the forbidden reflections for the space group *Imma* of wadsleyite were all within the background level. Elliptical integration scheme [*Schultz et al.*, 2014] was used for all the aquisitons.

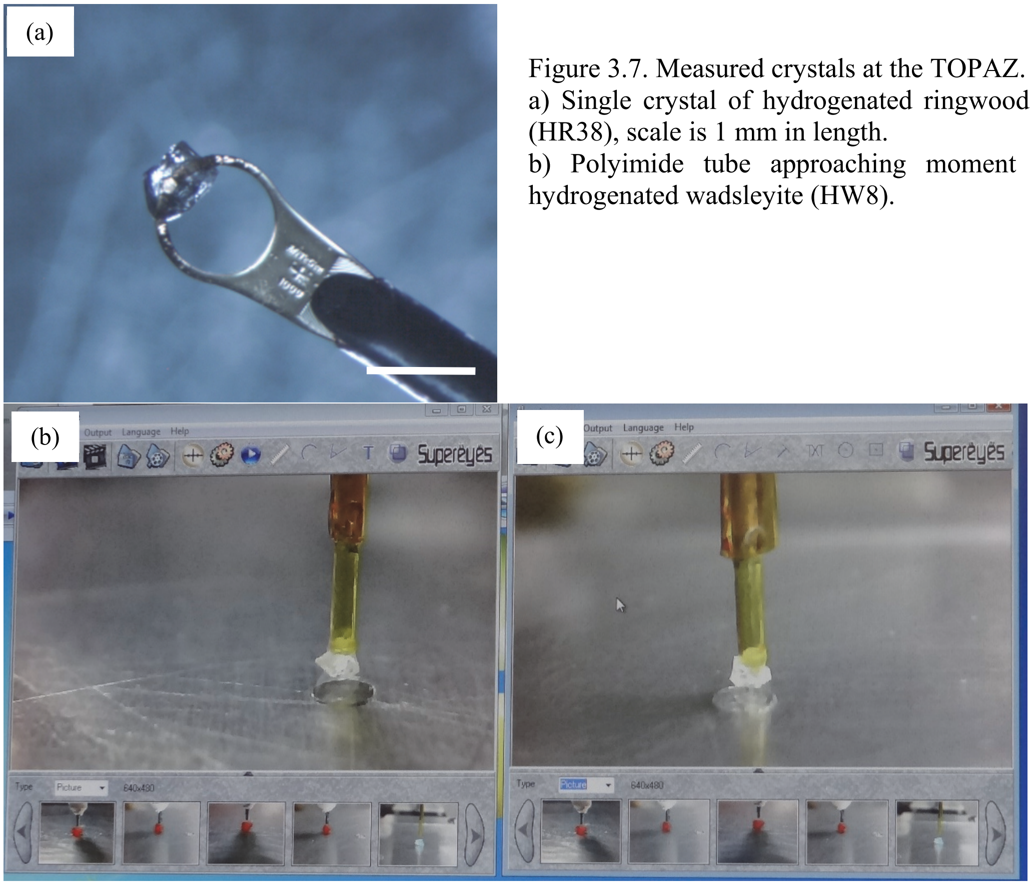

Figure 3.7. Measured crystals at the TOPAZ.
a) Single crystal of hydrogenated ringwoodite (HR38), scale is 1 mm in length.
b) Polyimide tube approaching moment to hydrogenated wadsleyite (HW8).

IV. STRUCTURE ANALYSIS

IV.1. Rietveld refinement

The obtained datasets of powder and single-crystal neutron diffraction were refined by using the Rietveld method. The Rietveld method is a structure refinement procedure and it uses the least squares fitting. The goal of this method is to achieve the best agreement between the observed diffraction intensities and those calculated from the structure model. This method provides quantitative structure parameters by enabling to refine many parameters simultaneously, which includes atomic coordinates, site occupancies and temperature factors (Debye-Waller factors). Before starting Rietveld refinement, space group and lattice constants of that phase must be known. The quality of a refinement is evaluated by R – factors. Generally, R_{wp}, R_e and χ^2 factors are considered. R_{wp} is weighted profile, which follows directly from the square root of the quantity minimized, scaled by the weighted intensities: $R_{wp}{}^2 = \Sigma_i w_i(y_{C,i} - y_{O,i})^2 / \Sigma_i w_i(y_{O,i})^2$, where weight labeled as w_i , $y_{C,i}$ is simulated from the model and $y_{O,i}$ is observed intensity values. R_e is expected R factor and it is equal with the $R_e = N / \Sigma_i w_i(y_{O,i})^2$, where N is number of data points. χ^2 is goodness of fit and it can be determined from the expected and weighted profile R factors $\chi^2 = (R_{wp}/R_e)^2$.

IV.2. Powder and single-crystal neutron diffraction data analyses

IV. 2.1. Powder neutron diffraction dataset

The obtained powder pattern of deuterated ringwoodite was analyzed by using the "Z-Rietveld" code [*Oishi et al.*, 2009], which was provided from J-PARC. The obtained pattern had more than 60 reflections with sufficient ratio of signal to background. We successfully refined the diffraction pattern by Rietveld method, which is shown in Figure 4.1. We also found a trace amount of brucite mixed with deuterated ringwoodite. We refined the structure parameters and mass ratio of that brucite through the refinement. The lattice constant of the deuterated ringwoodite was obtained from the PXRD result. Initial structure parameters except for D in ringwoodite were referred to single crystal X-ray results for ringwoodite [*Smyth et al.*, 2003] and neutron results for brucite [*Okuchi et al.*, 2014]. These parameters have been proven as very reliable and were not modified until the very final stage of the refinement. The Mg to Fe molar ratios of the coexisting two phases were always kept at Fo_{91}. After refining the structure parameters of Mg^{2+}, Fe^{2+}, Si^{4+} and O, we focused the refinement for finding D position.

Due to the cubic space group of ringwoodite ($Fd\bar{3}m$), there were several possible Wyckoff positions for D, which were 32*e*, 48*f*, 96*g*, 96*h* and 192*i*. Each candidate Wyckoff position was separately tested. The result will be given in later chapter. We refined isotropic Debye-Waller factors for Mg^{2+}, Fe^{2+}, Si^{4+} and O. In the case of D, we referred the previously reported isotropic Debye-Waller factor of D in deuterated wadsleyite [*Sano-Furukawa et al.*, 2011].

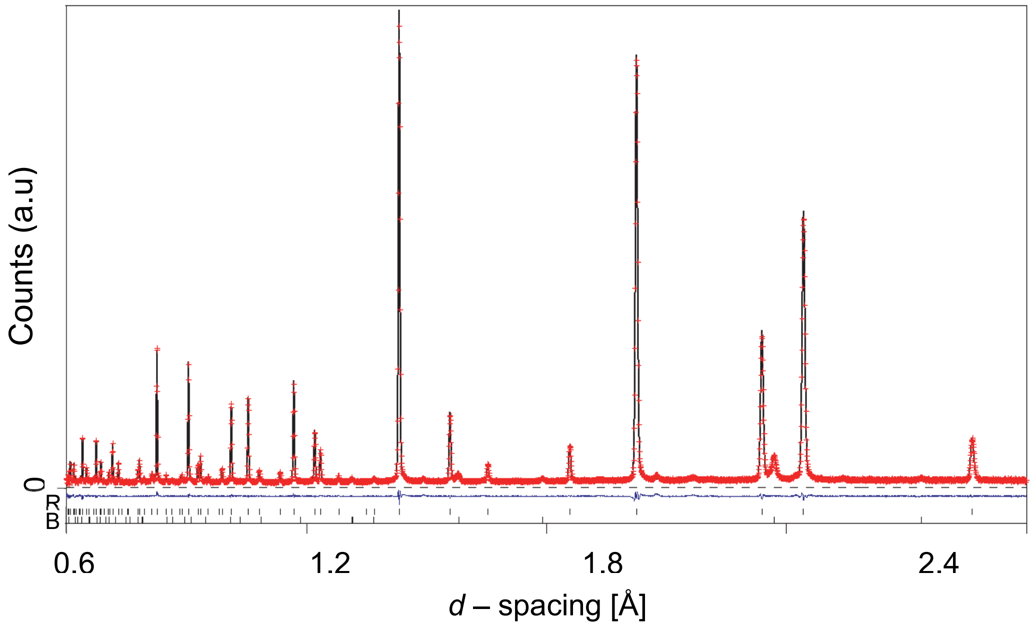

Figure 4.1. The time-of-flight neutron diffraction pattern of deuterated ringwoodite. Normalized counts without background subtraction are shown as crosses. The thin solid line shows the refined profile, and the dashed line shows the zero count position. The residual curve is shown below the zero count position. Tick with “R” and “B” symbols show Bragg reflections of ringwoodite and brucite, respectively.

IV.2.2. Single-crystal neutron diffraction datasets

The obtained single crystal neutron datasets were analysed by using the General Structure Analysis System (GSAS) [*Larson*, 2004]. We collected 2,149 reflections with minimum d-spacings (d_{min}) of 0.40 Å for hydrogenated ringwoodite at 100 K. We collected 10,795 reflections at 100 K, and 7,193 at 295 K, respectively, for hydrogenated wadsleyite. These reflections were with d_{min} of 0.30 Å. The intensity of all reflections were larger than 3σ uncertainty in their counting statistics. The observed reflection intensities are equal with the square of structure factor ($\Sigma F_{hkl}^{o2} = I_{hkl}$), where o denotes “observed”. We initially refined the structure parameters of Mg, Si and O atoms. Based on these refined parameters, we constructed calculated structure models (F_c) without H, where c denotes “calculated”. Then the calculated structure factors were subtracted from the observed structure factors ($|F^o| - |F^c|$) [*Wilson*, 2000], which generates difference of the structure factors. This difference is Fourier transformed into difference in the scattering density distribution ($\Delta\rho$), which follows the equation below:

$$\Delta\rho(xyz) = \sum_{hkl} (|F_{hkl}^{o}| - |F_{hkl}^{c}|)\exp\{-2\pi i(hx + ky + lz) + a_{hkl}^{c}\}$$

The $\Delta\rho(xyz)$ generated through this step is shown as the difference Fourier map. Initial H coordinates were taken from the analysis of all this map. Then we did additional refinements until the structure parameters including H are converged. Lattice constants of both phases were obtained from the single crystal neutron diffraction, which were used for the structure refinements. The secondary type I Lorentzian spread extinction model was applied for the structure refinements [*Jorgensen et al.*, 2014; *Larson*, 2004]. We did not set any constraint for the all the parameters during the refinements.

For hydrogenated ringwoodite, initial structure parameters were referred from our previous powder neutron diffraction study for deuterated ringwoodite except for H. All the parameters of each atom were refined separately. Then the initial hydrogen position was referred from the difference Fourier map. All the atoms were refined with isotropic Debye-Waller factors.

For hydrogenated wadsleyite, initial structure parameters of all atoms except for H were referred from the previous powder neutron diffraction for deuterated wadsleyite [*Sano-Furukawa et al.*, 2011]. Difference Fourier maps were generated at both temperatures. All the atoms were refined with anisotropic Debye-Waller factors. We performed additional refinements with variable d_{min} at 100 K data in order to confirm the refinement result.

V. HYDRATION MECHANISM OF RINGWOODITE

V.1. Background

Ringwoodite [$\gamma - (Mg,Fe)_2SiO_4$] is one of the two high-pressure polymorphs of olivine. It was first discovered in Tenham meteorite with composition of $(Mg_{0.66},Fe_{0.34})_2SiO_4$, which named after the Australian mineral physicist Ted Ringwood [*Binns*, 1969]. Later the first terrestrial ringwoodite was recovered as an inclusion in diamond [*Pearson et al.*, 2014]. It is the dominant phase occurring in the lover MTZ at depths between 525 km to 660 km, because it crystallizes at pressures between 18 and 23 GPa for mantle olivine of $(Mg_{0.91}Fe_{0.09})SiO_4$ composition [*Ito and Takahashi*, 1989; *Katsura and Ito*, 1989].

Ringwoodite has a cubic spinel type structure ($Fd\bar{3}m$) [*Kudoh et al.*, 2000; *Sasaki et al.*, 1982; *Smyth et al.*, 2004; *Smyth et al.*, 2003]. As mentioned in Chapter I, this structure has two types of polyhedral of oxygen atoms, which are octahedra (M sites) and tetrahedra (T sites). M sites have 16*d* and T sites have 8*a* Wyckoff positions at their centers as cations's sites, respectively. All these oxygen atoms are at 32*e* Wyckoff position. In addition, there is one vacant octahedra, which have a site at the center at 16*c* Wyckoff position.

As discussed already, ringwoodite is considered to be one of the largest reservoir of hidden water in the whole mantle system. It was reported that up to 3 wt.% of water in experimentally synthesized ringwoodite samples [*Kohlstedt et al.*, 1996; *Ye et al.*, 2012], while 1.4 wt.% of water was in the naturally occurred sample [*Pearson et al.*, 2014]. Many studies have focused on the effect of H_2O into physical properties of ringwoodite, while the hydrated crystal structure, especially position of hydrogen and its exchange mechanism with the other cations, has been left unclear. By previous single-crystal x-ray studies on hydrous ringwoodite, it was reported that principal hydration mechanism involves octahedral cation vacancies [*Kudoh et al.*, 2000; *Smyth et al.*, 2003], and the possible sites for hydrogen are between O–O pairs along the edges of 16*d* octahedra [*Kudoh et al.*, 2000]. First principle calculation studies predicted that the hydrogen might locate between two oxygens with the shortest O–O distances, which is at the shared edges of 16*d* and 16*c* octahedra [*Blanchard et al.*, 2009; *Kudoh et al.*, 2000; *Panero*, 2010; *Smyth et al.*, 2003]. However, actual crystallographic site and coordinates for hydrogen has been remained unclear. Thus, here we discuss the sites of hydrogen isotopes (both of hydrogen and deuterium) and their exchanging mechanisms with the other cation species in ringwoodite crystal structure, following our results of neutron diffraction.

V.2. Results

V.2.1. Deuterium sites in ringwoodite by powder neutron diffraction

The Refined structure parameters along the procedures in Chapter IV.2.1 are shown in Table 5.1. We observed that the D was simultaneously exchanged by Mg^{2+}, Fe^{2+} and Si^{4+} cations at both M and T sites, respectively. D atoms sites were found at the 192*i* and 96*g* Wyckoff positions, which were around M and T sites, respectively. As for more details of D positions, there are six equivalent sites around each corner (oxygen) of M sites and three equivalent sites around each corner (oxygen) of T sites. These sites are not possible to be completely occupied by D simultaneously. Following the site symmetries and local valence balances, there should be two D around one vacant M site and four D around one vacant T site (Figure 5.1). Those around M sites are approximately located along the shortest O–O distance pairs (2.86 Å) in the octahedron, with 1.30 Å in O–D (covalent bond) and 1.63 Å in O...D (hydrogen bond) lengths, and 154° in O–D…O hydrogen bonding angle. The D sites are located slightly outside of each vacant octahedron. On the other hand, D sites are located outside of tetrahedron faces with 1.00 Å in O–D distance and 127° in O–D…O angle.

Occupancies of Mg+Fe and Si at 16*d* and 8*a* positions should decrease with increasing D occupancies at 192*i* and 96*g* positions, because the averaged local valences around M and T sites were kept constrained at 2.0 and 4.0, respectively. The 0.34 pfu concentration of D atoms were only allowed to exchange either with Mg+Fe at M sites or with Si at T sites. We did not consider the cation disordering between M and T sites. The refinement was successfully converged at R_{wp} = 7.0 % and S (goodness of fit) = 1.59.

We also did refinements for two additional models as hypothetical end members. First, we assumed that all D atoms were at only 192*i*. Second, we assumed that all D atoms were at only 96*g*. Their R factors were much larger than the model of simultaneous occupancy of 192*i* and 96*g*. Therefore, that model was proved to be the most reliable (Table 5.2).

Table 5.1 Refined crystal structure parameters of deuterated ringwoodite.

Atoms	**Atomic coordinates**			**Occupancy**	U_{iso}**x10**^{2*}
	x	**y**	**z**		
Mg (16*d*)	0.5	0.5	0.5	0.8598(9)	0.58(1)
Fe (16*d*)	0.5	0.5	0.5	0.0850(1)	0.58(1)
Si (8*a*)	0.125	0.125	0.125	0.9702(10)	0.54(3)
O (32*e*)	0.24353(5)	0.24353(5)	0.24353(5)	1	0.67(1)
D (192*i*)	0.0382(17)	0.1111(19)	0.8582(24)	0.0092(2)	1.6$^{\#}$
D (96*g*)	0.2199(14)	0.2199(14)	0.1234(27)	0.0099(3)	1.6$^{\#}$

*Isotropic Debye-Waller factors; $^{\#}$From [*Sano-Furukawa et al.*, 2011]

Table 5.2. Comparison of D site models.

Models	R_{wp} **(%)**	R_{e} **(%)**	S
Only 192*i*	7.5	4.4	1.7
192*i* + 96*g*	7	4.4	1.59
Only 96*g*	7.7	4.4	1.75

As mentioned before, there was trace amount of brucite mixed with deuterated ringwoodite matrix. We refined mass fraction of this brucite. Its refined mass fraction was 1.3 wt.%, which was consistent with the molar ratio of (Mg+Fe)/Si = 1.97 in the coexisting ringwoodite, assuming the total mass-balance of Mg, Fe and Si within the sample capsule. This is very close to the refined ratio of the ringwoodite itself; (Mg+Fe)/Si = 1.95 for its bulk composition of $(\mathrm{Mg_{1.72}Fe_{0.17}D_{0.22}})(\mathrm{Si_{0.97}D_{0.12}})\mathrm{O_4}$. On the other hand, we expect the ratio (Mg+Fe)/Si = 1.83 for the M-site end member model of ringwoodite, which should coexist with ~7 wt.% of brucite, that is by far larger than its observed fraction.

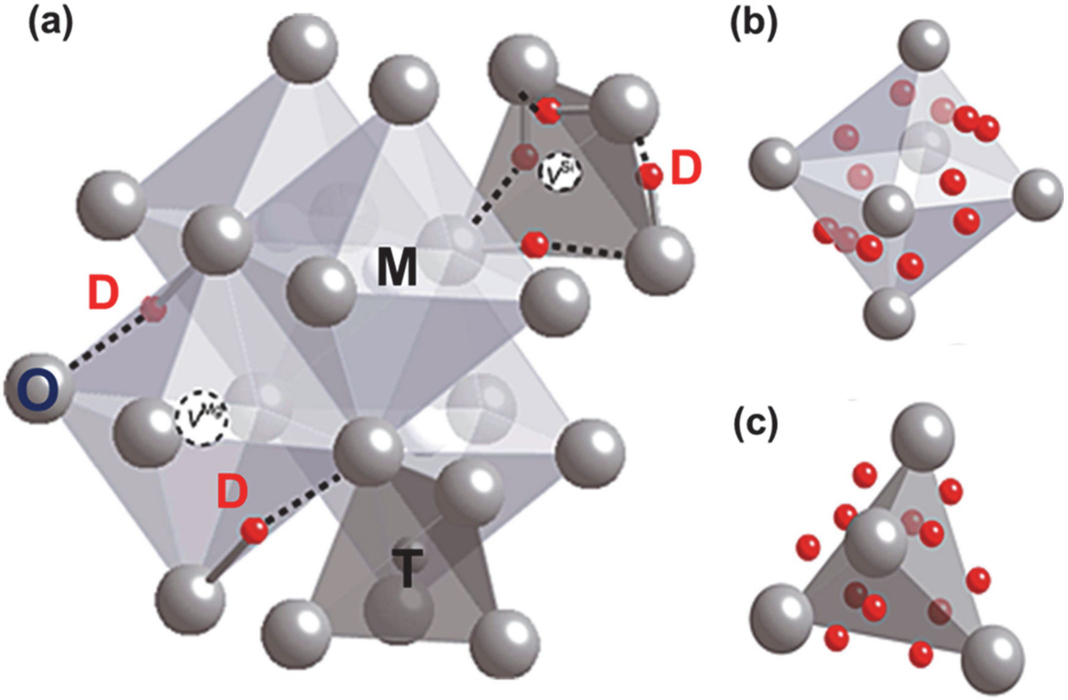

Figure 5.1. (a) Typical geometry of D atom positions in a local structure of ringwoodite. Thick dashed lines show hydrogen bonds. (b, c) Observed geometries of D atom sites at each M and T sites at 192*i* and 96*g* Wyckoff positions, respectively.

V.2.2. Hydrogen sites in ringwoodite by single-crystal neutron diffraction

Figure 5.2 shows the positions of H in the observed difference Fourier map around M site in ringwoodite structure. The H has negative scattering length density of neutron, while the other Mg, Si and O atoms all have positive scattering length density. The coordinates of the most intense negative residual was consistent with that of the D sites in the deuterated ringwoodite structure by powder neutron diffraction.

The H was at the 192*i* Wyckoff position around M site. The H located almost inside of the octahedron. The H atoms were exchanged by Mg^{2+} at M site. There are six equivalent H sites around each oxygen (Figure 5.3a). In order to keep the cation valence balances at M site, the two H must be substituted by one Mg^{2+} (Figure 5.3b).

Refined bond lengths were 1.10(3) Å for O–H and 1.80(3) Å for H…O. Bonding angle of O–H…O was 161°. The refined structure parameters are shown in Table 5.3. Structure refinement was converged at Rw(F) = 4.1 %, R(F) = 3.3% and $\chi^2 = 1.96$. The refined hydrogen occupancies corresponded to the composition of $(Mg_{1.929}H_{0.275})Si_{0.987}O_4$, where the total of all cation charges was slightly larger than that of the ideal stoichiometric value. We could not refine hydrogen occupancy at T site, which apparently seemed not consistent with the results of powder neutron diffraction for deuterium sites. However, we still clearly observed a substantial deficiency of the occupancy of Si at T site by this single crystal diffraction (Table 5.3). It suggested that the H must also be exchanged by Si at T site.

Table 5.3. Structure parameters of hydrogenated ringwoodite.

Atom	Atomic coordinates			Occupancy	U_{iso}x10^2*
	x	y	z		
Mg	0.5	0.5	0.5	0.965(1)	0.330(3)
Si	0.125	0.125	0.125	0.987(2)	0.252(5)
O	0.24396(1)	0.24396(1)	0.24396(1)	1	0.329(2)
H	0.355(5)	0.085(4)	0.018(4)	0.011(1)	4.0(6)

*Isotropic Debye-Waller factors

Lattice constants are a = 8.0786±3 Å and V = 527.234±36 Å^3, which were obtained from the neutron diffraction.

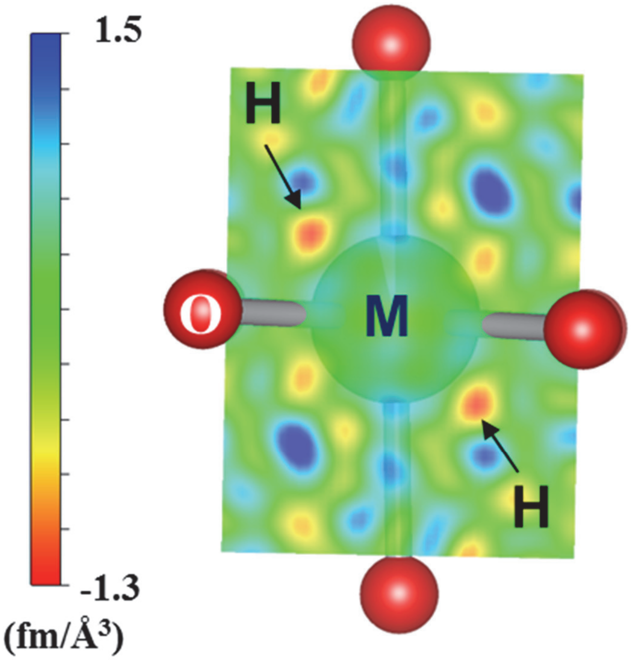

Figure 5.2. Difference Fourier map is showing the H atom in the local structure of ringwoodite. Slice is along (101) direction. The map was generated by using the dataset with d_{min} of 0.40 Å.

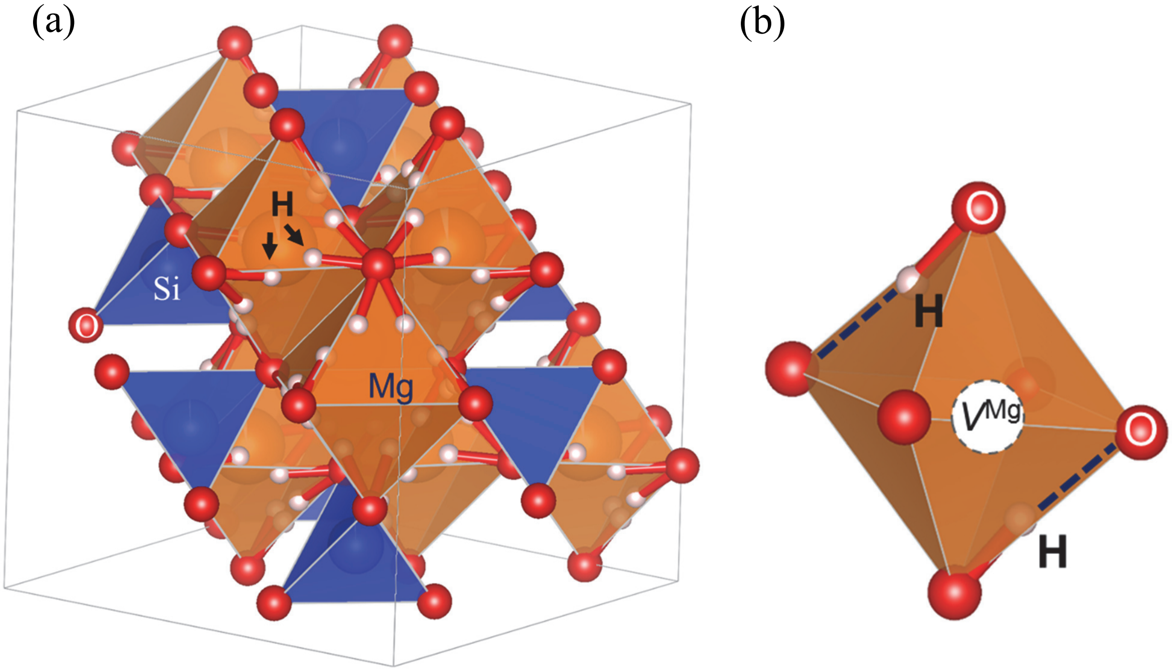

Figure 5.3. (a) Space-averaged structure of hydrous ringwoodite observed by neutron diffraction. (b) Ideal configuration of hydrogen atom in vacant octahedron.

V.3. Discussion

By using single-crystal neutron diffraction on hydrogenated ringwoodite, we obtained the reflection dataset with almost twice larger resolution in space than that of powder neutron diffraction on deuterated ringwoodite. We refined the D and H sites separately, in deuterated and hydrogenated ringwoodite crystal structures, respectively. Hydrogen or deuterium atoms in M sites are consistently located at $192i$ Wyckoff position, which was observed by both powder and single-crystal neutron diffraction. The both H and D atoms locate between the shortest O–O distance pairs along the edge of octahedron, which has 2.86 Å length in both deuterated and hydrogenated ringwoodite structures.

Deuterium atoms in T sites are located at $96g$ Wyckoff position, which was successfully refined only by powder neutron diffraction in deuterated ringwoodite. We could not refine the corresponding hydrogen atoms in T sites by using single-crystal neutron diffraction, while we observed substantial occupancy deficiency of Si at T site. That deficiency was larger than 3σ of the Si occupancy. It strongly suggests that the hydrogen must also be exchanged by Si cations at T sites, in addition to by Mg cations at M sites.

Refined bond length of O–H was shorter by 0.20 Å than that of O–D, while H…O was longer by 0.17 Å than that of H…O in the deuterated ringwoodite. Hydrogen bonding angle of O–H…O was larger by 7° than that of the deuterated ringwoodite. The H atoms were located slightly inside of octahedron compared with that of D atoms. These differences imply that the hydrogenated octahedron in H_2O-bearing ringwoodite had a larger volume than that of the deuterated octahedron in D_2O-bearing ringwoodite.

These observed geometries of both D and H atoms in the M sites of deuterated and hydrogenated ringwoodite structures were almost completely consistent with the prediction by first-principle calculations [*Blanchard et al.*, 2009; *Panero*, 2010]. The observed O–D bond length was larger by 0.3 Å than that of the predicted O–H bond length in M site [*Panero*, 2010], while the observed length of O–H was slightly longer by 0.08 Å. In the case of geometry of D in the T site of the deuterated ringwoodite structure, it was consistent with the prediction of Panero [2010]. The observed O–D bond length was 1.00 Å and it was within the predicted range of O–H bond length in T site, which was 0.97 – 1.02 Å [*Panero*, 2010].

From the viewpoint of crystal chemistry, it has been proposed that hydrogen cations exchange with Mg^{2+}, Fe^{2+} (at M) or Si^{4+} (at T) cations to form hydroxyls with surrounding oxygen anions [*Kudoh et al.*, 2000; *Smyth et al.*, 2003]. Because ionic valences are required to be compensated, each of Mg^{2+} or Fe^{2+} is exchanged with two hydrogens, as well as each of Si^{4+} is exchanged with four hydrogens. Therefore, two or four hydroxyl groups are expected to be clustered around each vacant M or T site, respectively [*Blanchard et al.*, 2009; *Panero*, 2010]. These expectations were confirmed by our present neutron diffraction study of hydrous ringwoodite.

VI. HYDRATION MECHANISM OF WADSLEYITE

VI.1. Background

Wadsleyite [$\beta - (Mg,Fe)_2SiO_4$] is the dominant phase presenting in the upper part of MTZ at depths between 410 km to 525 km, which is one of that two high pressure polymorphs of olivine. It has orthorhombic crystallographic symmetry with *Imma* space group, which is a modified-spinel type structure. As mentioned before, wadsleyite and ringwoodite show similar crystal structures, while the former has three distinct types of octahedra (M1, M2 and M3) in addition to single type of tetrahedra (T). These polyhedra are made of four types of oxygen sites (O1, O2, O3 and O4). Among these oxygens, O1 is particularly unique, because it does not connect with any Si^{4+}, while it has connected with five Mg^{2+} atoms.

Smyth [1987] predicted that O1 site is the most likely to hold significant amount of hydroxyl from the results of electrostatic and crystal-chemical calculations. By SIMS and infrared spectroscopy studies, it has been reported that wadsleyite hold up to 3 wt.% of water in its crystal structure [*Inoue et al.*, 1995; *Kohlstedt et al.*, 1996]. Previously, crystal structure of deuterated wadsleyite was studied by powder neutron diffraction, while the study was not conclusive for completely resolving hydrogen site and occupancy [*Sano-Furukawa et al.*, 2011]. They reported that there could be a missing hydrogen site in wadsleyite structure. That missing hydrogen site was suggested because of the difference of D_2O concentration, which was determined by structure refinement and lattice constant *b/a* ratio [*Jacobsen et al.*, 2005]. Here by TOF single-crystal Laue neutron diffraction, we unambiguously specified the cation species exchanging with H, as well as analysed the crystallographic site and occupancy of H in the structure of hydrogenated wadsleyite.

VI.2. Results

We refined the H site in wadsleyite using both 100 K and 295 K temperature neutron datasets. The observed difference Fourier maps clearly show the position of the largest negative scattering length density corresponding to H (Figure 6.1). The largest density was -5.3 fm/Å^3, which was almost three times larger than the two next largest negative residuals observed throughout all the datasets from $d_{\min}$ = 0.30 Å to $d_{\min}$ = 0.60 Å. The coordinates of the most intense negative residual was consistent with the previously reported Wyckoff position of deuterium atom in the deuterated wadsleyite [*Sano-Furukawa et al.*, 2011]. The largest negative density is therefore must be of the H. We emphasize that, except for this H site, no other excess scattering length density distribution was observed. (Figure 6.2).

The refined structure parameters of hydrogenated wadsleyite are shown in Tables 6.1 and 6.2. All atomic coordinates, including hydrogen, were refined using anisotropic Debye-Waller factors from the reflection intensity datasets (*hkl*) with the $d_{\min}$ of 0.30 Å. Our structure refinement results showed that there were four equivalent H^+ positions surrounding each of four equivalent O1 positions in the unit cell. While there was a total of 16 equivalent H^+ sites, it was found that these sites could not be simultaneously occupied (Figure 6.3a). It was determined that to maintain local valence balance, the two H^+ sites belonging to one empty M3 octahedron must be simultaneously occupied, where the octahedron consists of six oxygen atoms (two O1, two O3 and two O4). Each of these two H^+ was located along one of the two edges between the two O1– O4 pairs in that octahedron (Figure 6.3b). The refined bond length of O1–H was 0.999(5) Å at 100 K and 0.987(6) Å at 295 K. The difference between these O–H distances is well below the 3σ range and they are therefore nominally the same within their standard deviations.

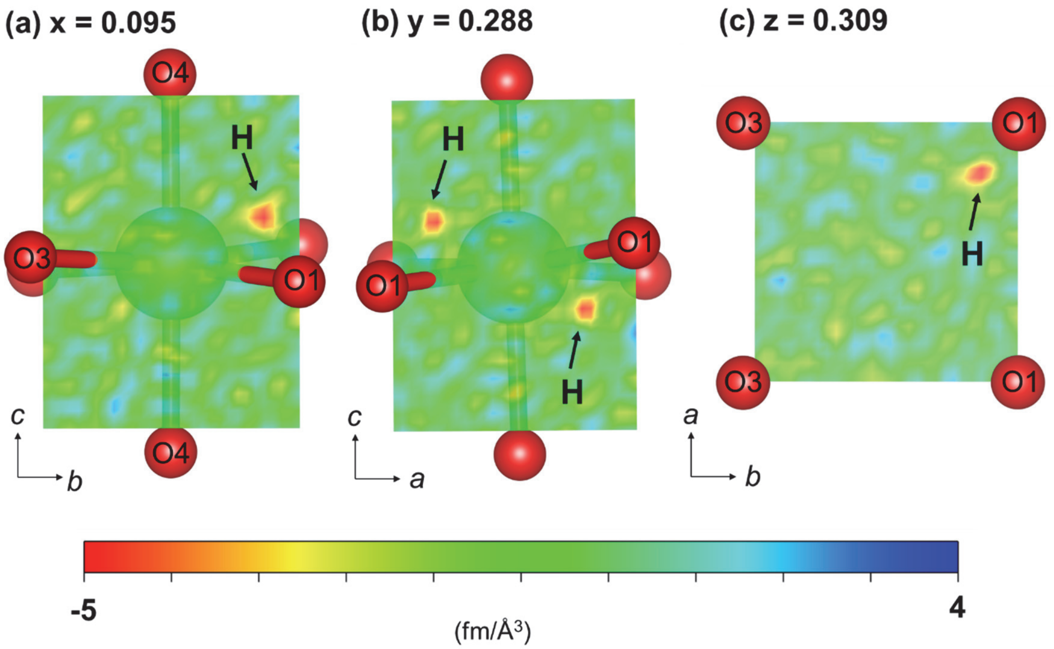

Figure 6.1. The difference Fourier maps are showing the hydrogen atom in the M3 site of hydrogenated wadsleyite from various orientation. The maps show the slices at (a) (100) section at *x* = 0.095, (b) (010) section at *y* = 0.288 and (c) (001) section at *z* = 0.309, respectively.

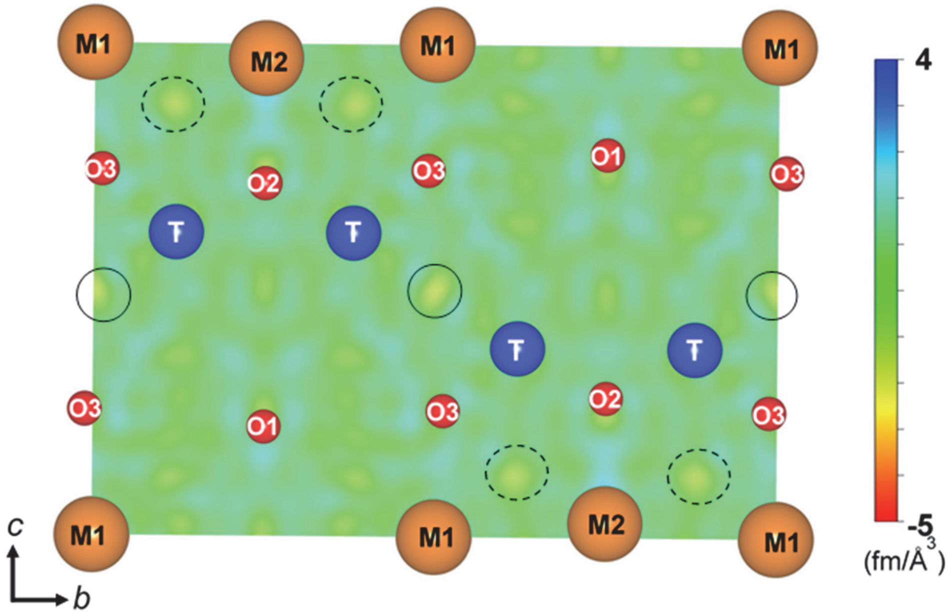

Figure 6.2. The difference Fourier map showing the positions of the other negative residuals. The map was generated from the difference of scattering length densities between the dataset with d_{min} = 0.6 Å and the refined structure model including the hydrogen. The solid and dashed circles are the positions of the residuals, which remained throughout all the difference Fourier maps constructed from several datasets with variable d_{min} from 0.30 Å to 0.60 Å. The other residuals are highly fluctuating as the d_{min} of the dataset was changing. The dashed circle at -1.65 fm/Å^3 is positioned at (x = 0; y = 0,6161; z = 0,1199). The solid circle at -2.02 fm/Å^3 is positioned at (x = 0,5; y = 0.0120; z = 0.0162). We consider that these residuals cannot be due to hydrogen, because the distances from these to their closest oxygen anions are 1.64 Å and 1.96 Å respectively, which are too long distances to form covalent chemical bonding.

Table 6.1. Structure parameters at 100 K.

Atom	***x/a***	***y/b***	***z/c***	**Occupancy**	**U_{11}x10^{2*}**	**U_{22}x10^{2*}**	**U_{33}x10^{2*}**	**U_{12}x10^{2*}**	**U_{13}x10^{2*}**	**U_{23}x10^{2*}**
Mg1	0	0	0	1.001(2)	0.764(12)	0.451(8)	0.942(10)	0	0	0.146(7)
Mg2	0	1/4	0.97043(4)	0.996(2)	0.581(1)	0.393(7)	0.408(7)	0	0	0
Mg3	1/4	0.12444(2)	1/4	0.895(1)	0.451(7)	0.831(7)	0.492(6)	0	-0.018(6)	0
Si	0	0.12039(2)	0.61624(3)	0.999(1)	0.375(7)	0.354(6)	0.368(6)	0	0	-0.011(5)
O1	0	1/4	0.22166(4)	1	0.416(9)	0.641(8)	0.708(8)	0	0	0
O2	0	1/4	0.71653(3)	1	0.591(9)	0.444(7)	0.404(7)	0	0	0
O3	0	0.98829(2)	0.25585(3)	1	0.591(7)	0.547(5)	0.463(5)	0	0	0.049(4)
O4	0.26055(3)	0.12332(1)	0.99392(2)	1	0.452(4)	0.495(3)	0.509(4)	-0.012(4)	0.031(3)	0.001(3)
H	0.0949(1)	0.2882(4)	0.3086(6)	0.105(2)	4.00(26)	3.42(20)	2.87(19)	-0.92(17)	-0.42(20)	-0.79(15)

*U_{ij} is anisotropic Debye-Waller factors

Lattice constants are a = 5.6810±2 Å, b = 11.4832±3 Å, c = 8.2541±3 Å and V = 538.458±27 Å^3, which were obtained from the neutron diffraction.

Table 6.2. Structure parameters at 295 K.

Atom	***x/a***	***y/b***	***z/c***	**Occupancy**	**U_{11}x10^{2*}**	**U_{22}x10^{2*}**	**U_{33}x10^{2*}**	**U_{12}x10^{2*}**	**U_{13}x10^{2*}**	**U_{23}x10^{2*}**
Mg1	0	0	0	1.000(2)	0.983(15)	0.598(10)	1.186(13)	0	0	0.111(8)
Mg2	0	1/4	0.97011(5)	0.997(2)	0.802(13)	0.540(9)	0.612(10)	0	0	0
Mg3	1/4	0.12437(3)	1/4	0.898(1)	0.598(9)	1.030(8)	0.724(8)	0	-0.058(7)	0
Si1	0	0.12042(3)	0.61613(4)	1.001(2)	0.503(8)	0.478(7)	0.494(8)	0	0	-0.015(6)
O1	0	1/4	0.22140(5)	1	0.538(11)	0.807(9)	0.900(11)	0	0	0
O2	0	1/4	0.71627(4)	1	0.824(11)	0.550(8)	0.548(9)	0	0	0
O3	0	0.98818(2)	0.25595(3)	1	0.742(8)	0.712(6)	0.627(7)	0	0	0.093(5)
O4	0.26076(3)	0.12330(2)	0.99382(2)	1	0.583(5)	0.653(4)	0.699(5)	-0.014(5)	0.067(4)	-0.003(3)
H	0.0933(2)	0.2873(5)	0.3076(8)	0.081(2)	3.42(32)	2.56(20)	2.04(23)	-0.73(19)	-0.13(22)	-0.58(18)

*U_{ij} is anisotropic Debye-Waller factors

Lattice constants are a = 5.6854±1 Å, b = 11.4829±2 Å, c = 8.2615±2 Å and V = 539.349±20 Å^3, which were obtained from the neutron diffraction.

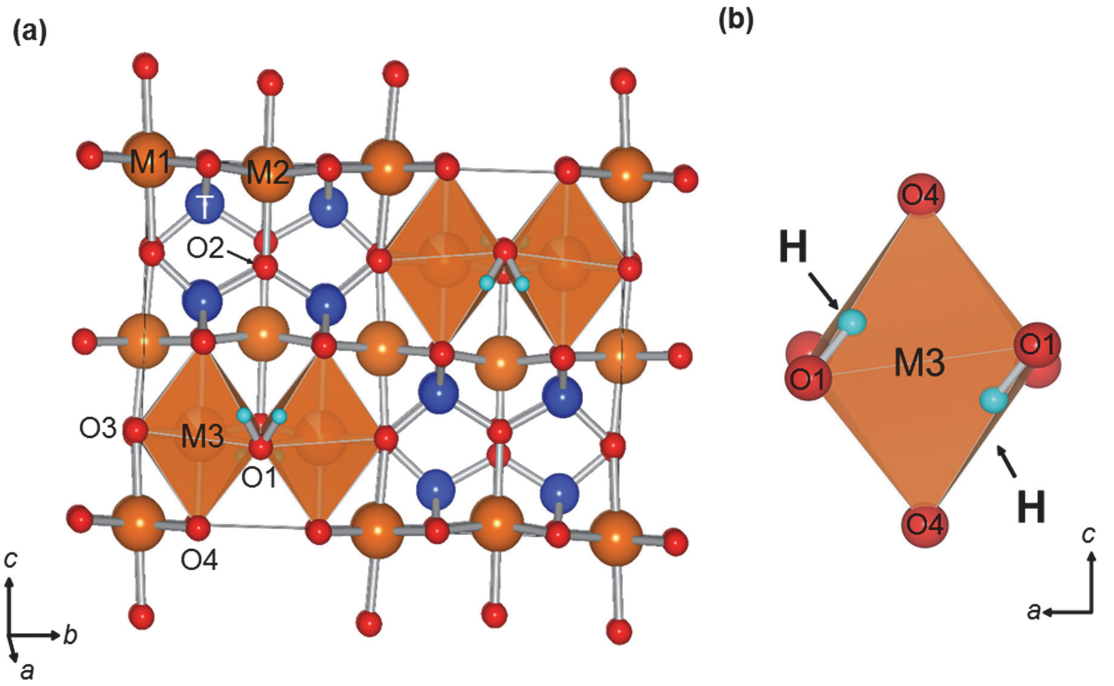

Figure 6.3. Visualization of hydrogen atom in the crystal structure of wadsleyite. (a) Observed geometry of hydrogen atom in wadsleyite framework. (b) Ideal configuration of hydrogen atom in near M3 local structure.

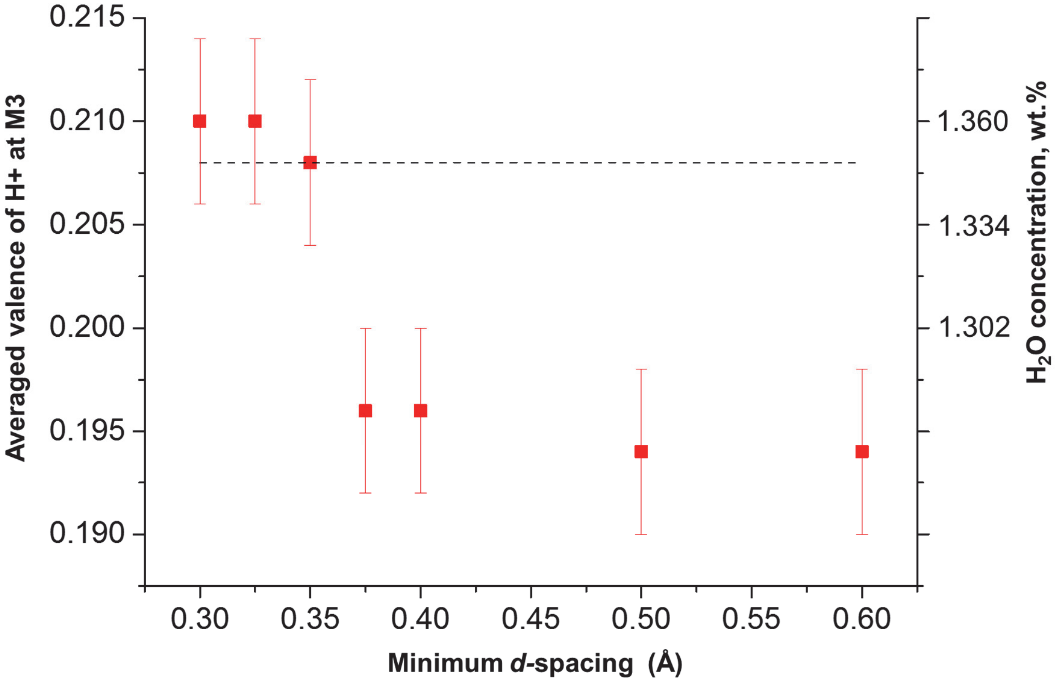

Figure 6.4. Observed valence of hydrogen at M3 site as a function of d_{min}. The dashed line is the charge of hydrogen independently estimated from that of lattice constant ratio *b/a* [*Jacobsen et al*., 2005].

In order to verify this hydrogen occupancy, we made additional refinements using datasets at 100 K with variable d_{min}. Then we compared the occupancy of the H^+ obtained from each refinement. Figure 6.4 shows the valence of H^+ at the M3 site as a function of d_{min}, which was calculated from the refined occupancies deduced from the datasets of variable d_{min}. Where the d_{min} was smaller than 0.325 Å, the observed valence of hydrogen became constant, whereas where the d_{min} was larger than 0.350 Å, the valence was depending on d_{min}. The amount of H^+ on the M3 site was converged to a partial occupancy of 0.105(2). The sum of the charge of Mg^{2+} and H^+ at M3 at $d_{min} \leq 0.325$ Å was 2.000(4), which is equal with its stoichiometric value. Thus, the constant charge of H^+ with d_{min} at 0.30 Å to 0.325 Å at 100 K was proven to be reliable.

As mentioned in Chapter II.4.1.3, the lattice constant ratio *b/a* is useful for independent evaluation of H_2O concentrations within the wadsleyite. The determined water concentration through this manner was converted into the valence of H^+, where we assumed that all the hydrogen is only in M3 site (dashed line in Figure 6.4). Then the converted valence of H^+ of our wadsleyite sample matched exactly the value deduced from the refined hydrogen occupancies found via neutron diffraction. Therefore, all hydrogen cations in the crystal (which collectively affect *b/a*) should have been fully concentrated into the M3 cavity. In other words, we confirmed that there are no other hydrogen sites. The maximum allowable concentration of H^+ in wadsleyite is constrained by its number of equivalent site of O1 oxygen, where there are equivalent four O1 site and each can connect with only one H. Thus at most four H can present in wadsleyite crystal structure, which corresponds to 3.33 wt.% of H_2O. It was also proposed by previous crystal chemical and SIMS analyses [*Inoue et al.*, 1995; *Smyth*, 1994].

We also refined the cation occupancies of Mg^{2+} at M1, M2, M3 and Si^{4+} at T sites, respectively. This refinement was carried out using the dataset at $d_{min} = 0.30$ Å at 100 K. The observed occupancies of these cations are converted into the valences, which results are shown in Figure 6.5. The valences of Mg^{2+} and Si^{4+} at M1, M2 and T sites were all equal with their stoichiometric values within the standard deviation of the refinement. The Mg^{2+} valence at M3 was significantly smaller than its stoichiometric value, whereas the sum of Mg^{2+} and H^{+} valences at M3 was equal to the stoichiometric value (shown as the dashed line).

The structure refinements were converged at $Rw(F) = 4.4$ %, $R(F) = 5.8$ % and $\chi^2 = 1.67$ for the 100 K dataset and at $Rw(F) = 4.4$ %, $R(F) = 6.2$ % and $\chi^2 = 1.60$ for the 295 K dataset. We finally evaluated the difference between these parameters before and after positioning of hydrogen atoms into the structure models, where the *Rw*(F) for the 100 K dataset was 5.1 % without hydrogen, while it was 4.4 % after refining the positioned hydrogen. Thus hydrogen was again proved to be incorporated in the given site. The Debye-Waller factors of all atoms at 100 K were substantially smaller than those at 295 K (Table 6.1 and 6.2). This is because thermal vibration of these atoms decreased with decreasing temperature, resulting in a more concentrated scattering length density distribution in space. In the case of hydrogen atoms, such concentration proved to be significant to improve the accuracy of the observed scattering length density and site occupancy of hydrogen.

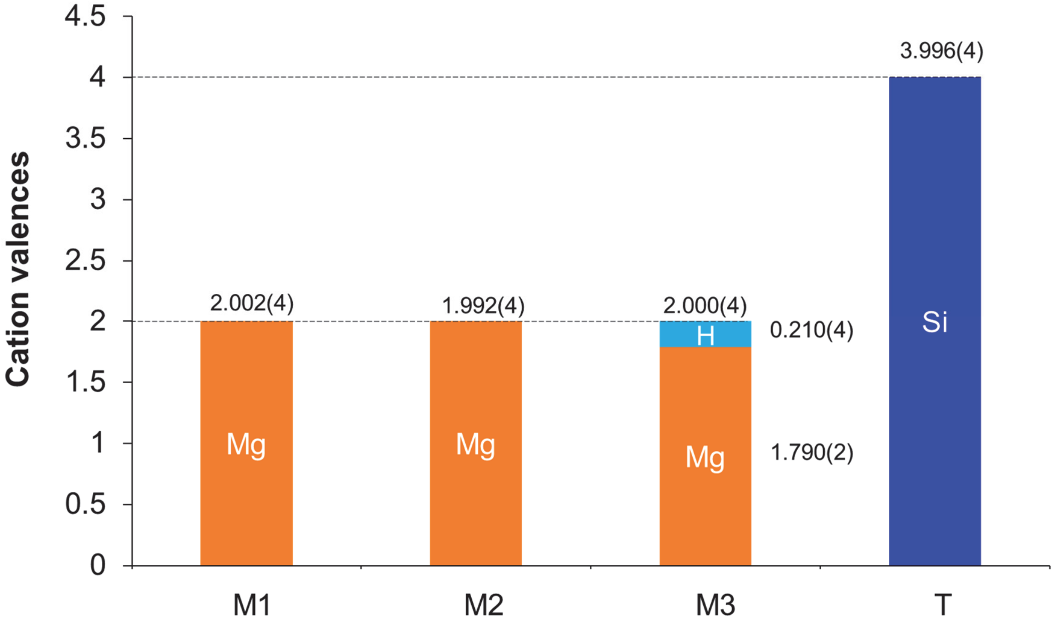

Figure 6.5. Observed valences of all cations at each site of the hydrous wadsleyite, which are calculated from the refined occupancies. The dashed line shows the stoichiometric values.

VI.3. Discussion

Our refined H site position was qualitatively consistent with the D site position the in deuterated wadsleyite [*Sano-Furukawa et al.*, 2011]. Compared with the deuterated wadsleyite, the positions of O1 and H are shifted slightly by 0.001 Å and 0.007 Å, respectively, in the same direction along the *c*-axis. Our observed O–H bond length at 295 K was 0.05 Å shorter than that of the O–D reported in the deuterated wadsleyite. The hydrogen bond lengths (O4…H) were 2.089(5) Å and 2.105(6) Å at 100 K and 295 K, respectively, where the latter is slightly longer than the former. The observed hydrogen bonding geometry was almost linear, with an O–H…O angle of 171° at both temperatures. The O4…H hydrogen bond at 295 K was 0.06 Å longer than that of O4…D in the deuterated wadsleyite, implying that the hydrogenated M3 octahedron had a slightly larger volume than that of the deuterated M3 octahedron.

The hydration of O1 oxygen site is consistent with previous studies of single-crystal x-ray diffraction, SIMS analysis, and IR spectroscopy [*Inoue et al.*, 1995; *Jacobsen et al.*, 2005; *Kudoh et al.*, 1996]. Our obtained IR spectra resembled typical spectrum of hydrous wadsleyite, which were reported previously [*Bolfan-Casanova et al.*, 2000; *Jacobsen et al.*, 2005]. Along with the results of the structure refinement, here we interpret the observed IR spectrum. Stretching vibration of OH with strong hydrogen bonding is observed at lower wavenumbers. In contrast, stretching vibration of OH with weak hydrogen bond is observed at higher wavenumbers. We observed the intense main band at around 3346 cm^{-1}, which may be caused by stretching vibration of OH with almost straight (O1–H…O4 bonding angle of 171°) hydrogen bond (O1…O4 distance is 3.082 Å). We also observed very weak band at around 3600 cm^{-1}, which may be caused stretching vibration of OH with bent (O1–H…O1 bonding angle of 112°) hydrogen bond (O1…O1 distance is 2.88 Å). Generally, it is observed that strong hydrogen bonds tend to be more linear, whereas weak ones are frequently bent [*Libowitzky and Beran*, 2006]. The distance of O1…O1 is much shorter than that of O1…O4, while this bent hydrogen bond of O1…O1 cannot be stronger than O1…O4. It is because each of that O1 is connected with H. Thus the two H atoms tend to repulse each other. There is expected geometry effect for hydrogen position due to the bent hydrogen bond, while we could not observe in our resolution. The concentration of bent hydrogen bonds are factor by several tens weaker than that of the straight hydrogen bond.

A recent study evaluating the chemical environment of H^+ in wadsleyite by nuclear magnetic resonance spectroscopy reported that some minor H^+ was bonded with oxygen O3 that belonged to Si^{4+} [*Griffin et al.*, 2013]. This finding is different from our results and may have resulted from different synthesis conditions. While their wadsleyite samples were synthesised in a solid state condition at relatively low temperatures from 1100 °C to 1200 °C, our crystals were grown in a partially-molten silicate melt at 1400 °C. The strain environment may have also been different, as our single crystal was grown under a hydrostatic condition in the melt, while the growth conditions of their powder samples are unknown. Accordingly, it is necessary to consider the effect of non-hydrostatic growth environments on the oxygen species, which were found to be bonding with a minor fraction of the hydrogen.

Additionally, there can be different hydrogen exchange mechanism in iron-bearing composition, where the hydrogen may also couple with Fe^{3+} to exchange for Si^{4+} at T sites [*Bolfan-Casanova et al.*, 2012; *Mrosko et al.*, 2015; *Smyth et al.*, 2014].

VII. WATER IN MANTLE TRANSITION ZONE

VII.1. Observed differences of physical properties between hydrous ringwoodite and hydrous wadsleyite

Wadsleyite and ringwoodite in the MTZ are unique because their water capacities are much larger than the other nominally anhydrous mantle minerals outside and inside the MTZ. The lower MTZ is considered to be extensively hydrated, at least in certain regions, as demonstrated by the recent discovery of natural hydrous ringwoodite [*Pearson et al.*, 2014]. Assuming that this water has been transported from the oceans, it would have passed through the upper MTZ to hydrate wadsleyite existing around its path.

As an example of the systematic differences in physical properties of wadsleyite and ringwoodite after their hydration, we summarised the decreasing trends of their bulk moduli as a function of H_2O concentration (Figure 7.1). All of these data points were taken from the previous experimental and theoretical studies on iron-free and iron-bearing wadsleyite and ringwoodite with various water concentrations [*Chang et al.*, 2015; *Hazen*, 1993; *Inoue et al.*, 1998; *Mao et al.*, 2008; *Mao et al.*, 2011; *Mao et al.*, 2012; *Sinogeikin et al.*, 1998; *Tsuchiya and Tsuchiya*, 2009; *Ye et al.*, 2012; *Yusa and Inoue*, 1997; *Yusa et al.*, 2000; *Zha et al.*, 1997]. We also included experimental and theoretical results for hydrous olivine as a reference [*Jacobsen et al.*, 2008; *Liu et al.*, 2009]. The bulk moduli of these mineral phases monotonically decrease with increasing water contents. Considering the similar crystal structures of wadsleyite and ringwoodite in their dry forms, they rather could have similar decreasing trends of the moduli upon hydration. However, the decreasing slope of ringwoodite is relatively steeper than that of wadsleyite and olivine. In addition, by previous studies it has been reported that iron-bearing hydrous ringwoodite has significantly larger $\Delta V_P/V_P$ and $\Delta V_S/V_S$ per unit H_2O concentration than those of hydrous wadsleyite, which were revealed by high-precision single crystal Brillouin scattering measured in situ at high pressure and temperature conditions [*Mao et al.*, 2012].

VII.2. Reason of the differences based on hydrogen substitution mechanism

The occurrence of simultaneous hydration of M and T sites in ringwoodite is in stark contrast compared with that of wadsleyite. It is because the hydration occurs only around one octahedral site (M3) in wadsleyite and there is no hydration in T site. By previous study, it was reported that the thermal expansion of T sites in hydrous ringwoodite were almost three times more significant that the expansion of its M site in same ringwoodite [*Ye et al.*, 2012]. Considering that the corresponding T sites in hydrous wadsleyite do not thermally expand at all [*Ye et al.*, 2011], the anomalous expansion should be exclusively related to the occurrence of T site hydration in hydrous ringwoodite; it is required to remind that T sites are not hydrated in hydrous wadsleyite, as well as that thermal expansion coefficients of hydrated M sites are comparable in both of these phases [*Ye et al.*, 2011; *Ye et al.*, 2012]. Therefore, the hydrated T sites should be the unique vulnerable points of hydrous ringwoodite. This may be the primary reason of that steep slope of bulk moduli sensitivity seen for ringwoodite than for wadsleyite (the two bulk moduli have a 15 GPa difference at zero H_2O concentration but become indistinguishable at greater than 2.0 wt.% H_2O) (Figure 7.1). The larger effect of hydration on ringwoodite than on wadsleyite was supported by a previous first principle study, where it was predicted that hydration of the tetrahedral sites is much more effective at reducing elastic properties than hydration of the octahedral sites [*Panero*, 2010]. In Figure 7.1, the dashed lines represent the theoretical calculations of wadsleyite and olivine, where the hydration mechanisms were assumed in both M sites in their crystal structures. It is clear that the theoretically calculated bulk moduli of wadsleyite and olivine are almost consistent with the experimentally obtained bulk moduli. Also the both decreasing bulk moduli trend of wadsleyite and olivine are similar, which indicates that the weakening of their chemical bonds occur at the same location in their minerals structures. On the other hand, in the case of ringwoodite, the simultaneous hydration of both M and T sites induces the softening the overall lattice and significantly reduces the corresponding seismic velocities as experimentally observed. Thus we propose that the difference of the bulk moduli slope between hydrous wadsleyite and hydrous ringwoodite are mainly induced by their differences in hydration mechanisms. It suggests that the best strategy to discover the hydrated region of lower and upper mantle transition zones can be qualitatively different each other. We conclude that 1.4 wt.% of H_2O in the recovered lower transition-zone ringwoodite [*Pearson et al.*, 2014] is easier to be seismologically detected than comparable or even higher concentration of H_2O in upper transition-zone wadsleyite [*Inoue et al.*, 2010], as long as spatial scale of such order of hydration is sufficiently large for the detection. The smaller effect of hydration on seismic velocities of wadsleyite at high pressures [*Mao et al.*, 2011] is consistent with this idea, although high-temperature measurements are yet to be conducted to evaluate the actual degree of difference between wadsleyite and ringwoodite. Considering that, the seismological evidences in lower transition zone areas indicated less order of H_2O concentrations in ringwoodite (~0.1 wt.%) [*Mao et al.*, 2012], we conclude that, its extensive hydration phenomenon (e.g., >1 wt.%) is more localized and to be detected by future studies with advanced multi-disciplinary approaches to integrate seismic profiles with magnetotelluric, electrical conductivity, as well as rheology and mantle dynamics studies [*Pommier*, 2014; *Schmandt et al.*, 2014]. Electromagnetic induction constraints are consistent with some hydration of transition zone areas while are still not very conclusive [*Kelbert et al.*, 2009; *Khan and Shankland*, 2012] partly because experimental results of laboratory conductivity measurements are not very consistent each other [*Huang et al.*, 2005; *Yoshino et al.*, 2008]. However, hydrous ringwoodite was observed to be always much more conductive than hydrous wadsleyite, which consistently suggests that proton translation in the former is much easier than the latter. This difference is naturally expected as the effect of hydration of T sites which work as “relay points” of protons; theoretical treatments considering the effect of T site hydration would be useful to evaluate the accurate conductivity of hydrous ringwoodite, as well as to evaluate the degree of conductivity difference between wadsleyite and ringwoodite. Such discussions from the viewpoints of atomistic-scale hydration mechanisms plays a promised role to understand geophysical and geochemical consequences of mantle transition-zone hydration phenomena.

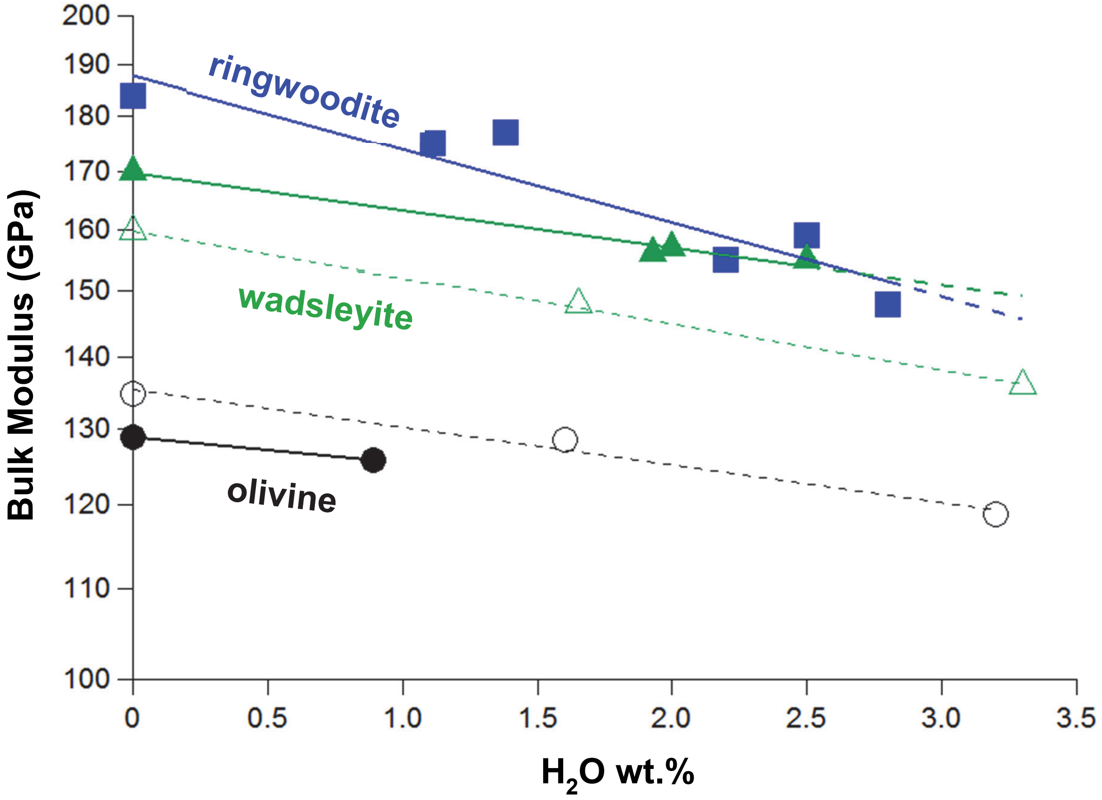

Figure 7.1. Experimental and theoretical results showing decreasing bulk moduli as a function of increasing water concentration. Triangles, squares and circles represent wadsleyite, ringwoodite and olivine results, respectively. All filled symbols represent previous experimental results. The open triangles and open circles represent density functional theory results for olivine and wadsleyite, respectively, where all hydrogen cations were positioned at M sites by exchanging for Mg^{2+}. The vertical axis is shown in the log scale.

VIII. CONCLUSION

VIII. Conclusion

1. We newly optimized a scaled-up Kawai type cells 14/8 and 18/10, which are suitable for synthesizing the required quality samples for neutron diffraction measurements.
2. We successfully applied a slow-cooling method at pressures up to 21 GPa for growing deep mantle hydrous minerals with high quality.
3. Hydration mechanism in ringwoodite structure was analyzed by powder and single-crystal neutron diffraction.
4. By powder neutron diffraction study of deuterated ringwoodite, we demonstrated that the deuterium atoms simultaneously exchanged with magnesium, iron and silicon cations, which were occupying both of M and T sites in the ringwoodite crystal structure.
5. By single-crystal neutron diffraction study of hydrogenated ringwoodite, we clearly observed that hydrogen atoms were exchanged with magnesium cation in M sites, while we could not refine hydrogen atoms in T sites. However, significant occupancy deficiency of silicon was observed in the T site, which strongly suggested that hydrogen must also be exchanged with silicon cations, in addition to the magnesium cations. This result is consistent with the powder neutron diffraction result of the iron-bearing deuterated ringwoodite.
6. By single-crystal neutron diffraction study of hydrogenated wadsleyite, we demonstrated that hydrogen in wadsleyite exchanged only with magnesium cation at M3 site, while it did not exchange with magnesium cation at the other M sites or silicon cation at T site.
7. We found the unique potential of single-crystal neutron diffraction for quantitative analysis of H_2O concentration in hydrous minerals.
8. We demonstrate that the hydration mechanisms between wadsleyite and ringwoodite are qualitatively different each other. Especially the hydration of T site in ringwoodite

is unique vulnerable point compared with that of not hydrated T site in wadsleyite. Thus, we propose that the difference of bulk moduli slope between hydrous wadsleyite and hydrous ringwoodite are mainly induced by their differences in hydration mechanisms.

9. Considering the difference of hydration mechanism between wadsleyite and ringwoodite, we conclude that the hydrated region of the upper and lower mantle transition zones can be qualitatively different each other. Moreover, the hydrated regions of lower mantle transition zone are easier to be seismologically detected than that of the hydrated region of upper mantle transition zone.

ACKNOWLEDGEMENTS

This doctoral research was carried out at the Institute for Planetary Materials (IPM), Okayama University, under the guidance of Dr. Takuo Okuchi. This doctoral research was made possible with help of dozens of people.

Firstly, I would like to express my grateful appreciation to my academic supervisor, Dr. Takuo Okuchi for his supervision, guidance, patience and continuous support. I also would to express my deep gratitude for my former supervisor Dr. Naotaka Tomioka for his guidance, teaching and patience.

I would like to say thanks to Chikako Oka and Dr. Akira Shimojuku for their technical supports for the high pressure synthesis experiments. Many thanks go to Dr. Jun Abe and Dr. Stefanus Harjo for their technical help for conducting powder neutron diffraction at TAKUMI, J-PARC.

My special thanks go to Dr. Christina Hoffmann and Dr. Xiaoping Wang for their technical supports for conducting single crystal neutron diffraction and as well as their guidance for analyzing the neutron dataset at ORNL. I also would like to thanks to Junhong Helen He for the sample handling.

I would like to express my big thanks to Dr. Shigeru Yamashita for the FTIR sample preparation and measurements. My special thanks go to Prof. Jung-Fu Lin for the discussion of last Misasa-VI conference presentation. I would like to say thank you to Prof. Masami Kanzaki for the discussion of structure refinement. I like to say thank you to Hacto members for their help and kindness.

I am grateful to my mother, Shirchinjav Tumenbayar, to my second oldest sister Narantuya Purevjav and to all my family members, for their continuous encouragement and advices throughout my studies.

I would like to say big thank you to Eiji Ito for his humble personality and help me in numerous ways. I express my thanks to my friends Fang Xu, Ivan Pineda Velasco and Longjian Xie for their support and kindness. I like to convey my special thanks to Matsubara Fumie for her help in numerous ways in my daily life. My special thanks go to Masako Uyama, who always encourage me. Finally, I want to thank all the colleagues and stuff of IPM for their assistance and support in numerous ways. Part of this research was supported by JSPS KAKENHI Grant number 15J03633.

LIST OF TABLES

LIST OF FIGURES

REFERENCES

Akaogi, M., E. Ito, and A. Navrotsky (1989), Olivine-modified spinel-spinel transitions in the system Mg_2SiO_4-Fe_2SiO_4 - Calorimetric measurements, thermochemical calculation, and geophysical application, *J Geophys Res-Solid*, *94*(B11), 15671-15685.

Ashbrook, S. E., A. J. Berry, W. O. Hibberson, S. Steuernagel, and S. Wimperis (2005), High-resolution O-17 MAS NMR spectroscopy of forsterite (α-Mg_2SiO_4) wadsleyite (β-Mg_2SiO_4), and ringwoodite (γ-Mg_2SiO_4), *Am Mineral*, *90*(11-12), 1861-1870.

Bebout, G. E. (1996), Volatile transfer and recycling at convergent margins: mass-balance and insights from high-P/T methamorphic rocks.

Benz, H. M., and J. E. Vidale (1993), Sharpness of upper-mantle discontinuities determined from high-frequency reflections, *Nature*, *365*(6442), 147-150.

Bercovici, D., and S. Karato (2003), Whole-mantle convection and the transition-zone water filter, *Nature*, *425*(6953), 39-44.

Binns, R. A., Davis, R. J., and Reed, S. J. B (1969), Ringwoodite, natural $(Mg,Fe)_2SiO_4$ spinel in the Tenham Meteorite, *Nature 221*, 943-944.

Blanchard, M., K. Wright, and J. D. Gale (2005), A computer simulation study of OH defects in Mg_2SiO_4 and Mg_2GeO_4 spinels, *Phys. Chem. Miner.*, *32*(8-9), 585-593.

Blanchard, M., E. Balan, and K. Wright (2009), Incorporation of water in iron-free ringwoodite: A first-principles study, *Am Mineral*, *94*(1), 83-89.

Blanchard, M., M. Roberge, E. Balan, G. Fiquet, and H. Bureau (2013), Infrared signatures of OH-defects in wadsleyite: A first-principles study, *Am Mineral*, *98*(11-12), 2132-2143.

Bolfan-Casanova, N., H. Keppler, and D. C. Rubie (2000), Water partitioning between nominally anhydrous minerals in the MgO-SiO_2-H_2O system up to 24 GPa:

implications for the distribution of water in the Earth's mantle, *Earth and Planetary Science Letters*, *182*(3-4), 209-221.

Bolfan-Casanova, N., M. Munoz, C. McCammon, E. Deloule, A. Ferot, S. Demouchy, L. France, D. Andrault, and S. Pascarelli (2012), Ferric iron and water incorporation in wadsleyite under hydrous and oxidizing conditions: A XANES, Mossbauer, and SIMS study, *Am Mineral*, *97*(8-9), 1483-1493.

Chang, Y. Y., et al. (2015), Comparative compressibility of hydrous wadsleyite and ringwoodite: Effect of H_2O and implications for detecting water in the transition zone, *J Geophys Res-Sol Ea*, *120*(12), 8259-8280.

Dai, L., and S. I. Karato (2009), Electrical conductivity of wadsleyite at high temperatures and high pressures, *Earth and Planetary Science Letters*, *287*(1-2), 277-283.

Dziewonski, A. M., and D. L. Anderson (1981), Preliminary reference earth model, *Phys Earth Planet In*, *25*(4), 297-356.

Frost, D. J., B. T. Poe, R. G. Tronnes, C. Liebske, A. Duba, and D. C. Rubie (2004), A new large-volume multianvil system, *Phys Earth Planet In*, *143*, 507-514.

Griffin, J. M., A. J. Berry, D. J. Frost, S. Wimperis, and S. E. Ashbrook (2013), Water in the Earth's mantle: a solid-state NMR study of hydrous wadsleyite, *Chem Sci*, *4*(4), 1523-1538.

Harjo, S., A. Moriai, S. Torii, H. Suzuki, K. Suzuya, Y. Morii, M. Arai, Y. Tomota, K. Akita, and Y. Akiniwa (2006), Design of engineering diffractometer at J-PARC, *Mater Sci Forum*, *524-525*, 199-204.

Hazen, R. M. (1993), Comparative compressibilities of silicate spinels - Anomalous behavior of $(Mg,Fe)_2SiO_4$, *Science*, *259*(5092), 206-209.

Holl, C. M., J. R. Smyth, S. D. Jacobsen, and D. J. Frost (2008), Effects of hydration on the structure and compressibility of wadsleyite, β-(Mg_2SiO_4), *Am Mineral*, *93*(4), 598-607.

Holland, T. J. B., and S. A. T. Redfern (1997), Unit cell refinement from powder diffraction data: The use of regression diagnostics, *Mineral Mag*, *61*(1), 65-77.

Huang, X. G., Y. S. Xu, and S. I. Karato (2005), Water content in the transition zone from electrical conductivity of wadsleyite and ringwoodite, *Nature*, *434*(7034), 746-749.

Inoue, T., H. Yurimoto, and Y. Kudoh (1995), Hydrous modified spinel, $Mg_{1.75}SiH_{0.5}O_4$ - A new water reservoir in the mantle transition region, *Geophys Res Lett*, *22*(2), 117-120.

Inoue, T., D. J. Weidner, P. A. Northrup, and J. B. Parise (1998), Elastic properties of hydrous ringwoodite (γ-phase) in Mg_2SiO_4, *Earth and Planetary Science Letters*, *160*(1-2), 107-113.

Inoue, T., T. Wada, R. Sasaki, and H. Yurimoto (2010), Water partitioning in the Earth's mantle, *Phys Earth Planet In*, *183*(1-2), 245-251.

Inoue, T., Y. Tanimoto, T. Irifune, T. Suzuki, H. Fukui, and O. Ohtaka (2004), Thermal expansion of wadsleyite, ringwoodite, hydrous wadsleyite and hydrous ringwoodite, *Phys Earth Planet In*, *143*, 279-290.

Ito, E., and E. Takahashi (1989), Postspinel Transformations in the System Mg_2SiO_4-Fe_2SiO_4 and Some Geophysical Implications, *J Geophys Res-Solid*, *94*(B8), 10637-10646.

Ito, E., D. M. Harris, and A. T. Anderson (1983), Alteration of oceanic-crust and geologic cycling of chlorine and water, *Geochim Cosmochim Ac*, *47*(9), 1613-1624.

Jacobsen, S. D., J. R. Smyth, H. Spetzler, C. M. Holl, and D. J. Frost (2004), Sound velocities and elastic constants of iron-bearing hydrous ringwoodite, *Phys Earth Planet In*, *143*, 47-56.

Jacobsen, S. D., S. Demouchy, D. J. Frost, T. B. Ballaran, and J. Kung (2005), A systematic study of OH in hydrous wadsleyite from polarized FTIR spectroscopy and single-crystal X-ray diffraction: Oxygen sites for hydrogen storage in Earth's interior, *Am Mineral*, *90*(1), 61-70.

Jacobsen, S. D., F. M. Jiang, Z. Mao, T. S. Duffy, J. R. Smyth, C. M. Holl, and D. J. Frost (2008), Effects of hydration on the elastic properties of olivine, *Geophys Res Lett*, *35*(14).

Jorgensen, M. R. V., V. R. Hathwar, M. Sist, X. P. Wang, C. M. Hoffmann, A. L. Briseno, J. Overgaard, and B. B. Iversen (2014), Accurate atomic displacement parameters from time-of-flight neutron-diffraction data at TOPAZ, *Acta Crystallogr A*, *70*, 679-681.

Katsura, T., and E. Ito (1989), The System Mg_2SiO_4- Fe_2SiO_4 at high-pressures and temperatures - precise determination of stabilities of olivine, modified spinel, and spinel, *J Geophys Res-Solid*, *94*(B11), 15663-15670.

Kelbert, A., A. Schultz, and G. Egbert (2009), Global electromagnetic induction constraints on transition-zone water content variations, *Nature*, *460*(7258), 1003-U1085.

Keppler, H. (2014), GEOLOGY Earth's deep water reservoir, *Nature*, *507*(7491), 174-175.

Khan, A., and T. J. Shankland (2012), A geophysical perspective on mantle water content and melting: Inverting electromagnetic sounding data using laboratory-based electrical conductivity profiles, *Earth and Planetary Science Letters*, *317*, 27-43.

Kohlstedt, D. L., H. Keppler, and D. C. Rubie (1996), Solubility of water in the α, β and γ phases of $(Mg,Fe)_2SiO_4$, *Contrib Mineral Petr*, *123*(4), 345-357.

Kohn, S. C., R. A. Brooker, D. J. Frost, A. E. Slesinger, and B. J. Wood (2002), Ordering of hydroxyl defects in hydrous wadsleyite (β-Mg_2SiO_4), *Am. Miner.*, *87*(2-3), 293-301.

Kudoh, Y., T. Inoue, and H. Arashi (1996), Structure and crystal chemistry of hydrous wadsleyite, $Mg_{1.75}SiH_{0.5}O_4$: Possible hydrous magnesium silicate in the mantle transition zone, *Phys Chem Miner*, *23*(7), 461-469.

Kudoh, Y., T. Kuribayashi, H. Mizobata, and E. Ohtani (2000), Structure and cation disorder of hydrous ringwoodite, γ-$Mg_{1.89}Si_{0.98}H_{0.30}O_4$, *Phys Chem Miner*, *27*(7), 474-479.

Larson, A. C., Von Dreele, R.B., (2004), General structure analysis system (GSAS), edited, pp. 86-748.

Lemaire, C., S. C. Kohn, and R. A. Brooker (2004), The effect of silica activity on the incorporation mechanisms of water in synthetic forsterite: a polarised infrared spectroscopic study, *Contrib Mineral Petr*, *147*(1), 48-57.

Li, L., J. Brodholt, and D. Alfe (2009), Structure and elasticity of hydrous ringwoodite: A first principle investigation, *Phys Earth Planet In*, *177*(3-4), 103-115.

Libowitzky, E., and A. Beran (2006), The structure of hydrous species in nominally anhydrous minerals: Information from polarized IR spectroscopy, *Reviews in Mineralogy and Geochemistry*, *62*(1), 29-52.

Liu, L., J. G. Du, J. J. Zhao, H. Liu, H. L. Gao, and Y. X. Chen (2009), Elastic properties of hydrous forsterites under high pressure: First-principle calculations, *Phys Earth Planet In*, *176*(1-2), 89-97.

Loeffert, A., C. Gross, and W. Assmus (2002), Crystal growth under high pressure: preparation of the spin-ladder compound SrCu2O3, *J Phys-Condens Mat*, *14*(44), 11161-11166.

Mao, Z., S. D. Jacobsen, F. Jiang, J. R. Smyth, C. M. Holl, and T. S. Duffy (2008), Elasticity of hydrous wadsleyite to 12 GPa: Implications for Earth's transition zone, *Geophys Res Lett*, *35*(21).

Mao, Z., S. D. Jacobsen, D. J. Frost, C. A. McCammon, E. H. Hauri, and T. S. Duffy (2011), Effect of hydration on the single-crystal elasticity of Fe-bearing wadsleyite to 12 GPa, *Am Mineral*, *96*(10), 1606-1612.

Mao, Z., J. F. Lin, S. D. Jacobsen, T. S. Duffy, Y. Y. Chang, J. R. Smyth, D. J. Frost, E. H. Hauri, and V. B. Prakapenka (2012), Sound velocities of hydrous ringwoodite to 16 GPa and 673 K, *Earth and Planetary Science Letters*, *331*, 112-119.

Momma, K., and F. Izumi (2011), VESTA 3 for three-dimensional visualization of crystal, volumetric and morphology data, *J Appl Crystallogr*, *44*, 1272-1276.

Morishima, H., T. Kato, M. Suto, E. Ohtani, S. Urakawa, W. Utsumi, O. Shimomura, and T. Kikegawa (1994), The Phase-Boundary between α-Mg_2SiO_4 and β-Mg_2SiO_4 Determined by in-Situ X-Ray-Observation, *Science*, *265*(5176), 1202-1203.

Mrosko, M., M. Koch-Muller, C. McCammon, D. Rhede, J. R. Smyth, and R. Wirth (2015), Water, iron, redox environment: effects on the wadsleyite-ringwoodite phase transition, *Contrib Mineral Petr*, *170*(1).

Ohtani, E., K. Litasov, T. Hosoya, T. Kubo, and T. Kondo (2004), Water transport into the deep mantle and formation of a hydrous transition zone, *Phys Earth Planet In*, *143*, 255-269.

Oishi, R., M. Yonemura, Y. Nishimaki, S. Torii, A. Hoshikawa, T. Ishigaki, T. Morishima, K. Mori, and T. Kamiyama (2009), Rietveld analysis software for J-PARC, *Nucl Instrum Meth A*, *600*(1), 94-96.

Okuchi, T., N. Purevjav, N. Tomioka, J. F. Lin, T. Kuribayashi, L. Schoneveld, H. Hwang, N. Sakamoto, N. Kawasaki, and H. Yurimoto (2015a), Synthesis of large and homogeneous single crystals of water-bearing minerals by slow cooling at deep-mantle pressures, *Am Mineral*, *100*(7), 1483-1492.

Okuchi, T., A. Hoshikawa, and T. Ishigaki (2015b), Forge-Hardened TiZr null-matrix alloy for neutron scattering under extreme conditions, *Metals-Basel*, *5*(4), 2340-2350.

Okuchi, T., N. Tomioka, N. Purevjav, J. Abe, S. Harjo, and W. Gong (2014), Structure refinement of sub-cubic-mm volume sample at high pressures by pulsed neutron powder diffraction: application to brucite in an opposed anvil cell, *High Pressure Res*, *34*(2), 273-280.

Okuchi, T., M. Yoshida, Y. Ohno, N. Tomioka, N. Purevjav, T. Osakabe, S. Harjo, J. Abe, K. Aizawa, and S. Sasaki (2013), Pulsed neutron powder diffraction at high pressure by a capacity-increased sapphire anvil cell, *High Pressure Res*, *33*(4), 777-786.

Panero, W. R. (2010), First principles determination of the structure and elasticity of hydrous ringwoodite, *J Geophys Res-Sol Ea*, *115*.

Peacock, S. M. (1990), Fluid Processes in Subduction Zones, *Science*, *248*(4953), 329-337.

Pearson, D. G., et al. (2014), Hydrous mantle transition zone indicated by ringwoodite included within diamond, *Nature*, *507*(7491), 221.

Pommier, A. (2014), Interpretation of Magnetotelluric Results Using Laboratory Measurements, *Surv Geophys*, *35*(1), 41-84.

Purevjav, N., T. Okuchi, N. Tomioka, J. Abe, and S. Harjo (2014), Hydrogen site analysis of hydrous ringwoodite in mantle transition zone by pulsed neutron diffraction, *Geophys Res Lett*, *41*(19), 6718-6724.

Purevjav, N., T. Okuchi, N. Tomioka, X. P. Wang, and C. Hoffmann (2016), Quantitative analysis of hydrogen sites and occupancy in deep mantle hydrous wadsleyite using single crystal neutron diffraction, *Sci Rep-Uk*, *6*.

Revenaugh, J., and S. A. Sipkin (1994), Seismic evidence for silicate melt atop the 410 km mantle discontinuity, *Nature*, *369*(6480), 474-476.

Sano-Furukawa, A., T. Kuribayashi, K. Komatsu, T. Yagi, and E. Ohtani (2011), Investigation of hydrogen sites of wadsleyite: A neutron diffraction study, *Phys Earth Planet In*, *189*(1-2), 56-62.

Sasaki, S., C. T. Prewitt, Y. Sato, and E. Ito (1982), Single-crystal x-ray study of γ-Mg_2SiO_4, *J Geophys Res*, *87*(Nb9), 7829-7832.

Schmandt, B., S. D. Jacobsen, T. W. Becker, Z. X. Liu, and K. G. Dueker (2014), EARTH'S INTERIOR Dehydration melting at the top of the lower mantle, *Science*, *344*(6189), 1265-1268.

Schultz, A. J., M. R. V. Jorgensen, X. P. Wang, R. L. Mikkelson, D. J. Mikkelson, V. E. Lynch, P. F. Peterson, M. L. Green, and C. M. Hoffmann (2014), Integration of neutron time-of-flight single-crystal Bragg peaks in reciprocal space, *J Appl Crystallogr*, *47*, 915-921.

Shatskiy, A., K. D. Litasov, T. Matsuzaki, K. Shinoda, D. Yamazaki, A. Yoneda, E. Ito, and T. Katsura (2009), Single crystal growth of wadsleyite, *Am Mineral*, *94*(8-9), 1130-1136.

Shatskiy, A., D. Yamazaki, Y. M. Borzdov, T. Matsuzaki, K. D. Litasov, T. Cooray, A. Ferot, E. Ito, and T. Katsura (2010), Stishovite single-crystal growth and application to silicon self-diffusion measurements, *Am Mineral*, *95*(1), 135-143.

Shatskiy, A., T. Katsura, K. D. Litasov, A. V. Shcherbakova, Y. M. Borzdov, D. Yamazaki, A. Yoneda, E. Ohtani, and E. Ito (2011), High pressure generation using scaled-up Kawai-cell, *Phys Earth Planet In*, *189*(1-2), 92-108.

Shearer, P. M. (1990), Seismic imaging of upper-mantle structure with new evidence for a 520-km discontinuity, *Nature*, *344*(6262), 121-126.

Sinogeikin, S. V., T. Katsura, and J. D. Bass (1998), Sound velocities and elastic properties of Fe-bearing wadsleyite and ringwoodite, *J Geophys Res-Sol Ea*, *103*(B9), 20819-20825.

Smyth, J. R. (1987), β-Mg_2SiO_4 - A potential host for water in the mantle, *Am Mineral*, *72*(11-12), 1051-1055.

Smyth, J. R. (1994), A Crystallographic Model for Hydrous Wadsleyite (β-Mg_2SiO_4) - an Ocean in the Earths Interior, *Am Mineral*, *79*(9-10), 1021-1024.

Smyth, J. R., and S. D. Jacobsen (2006), Nominally anhydrous minerals and Earth's deep water cycle, *Geophysical Monograph 168*.

Smyth, J. R., C. M. Holl, D. J. Frost, and S. D. Jacobsen (2004), High pressure crystal chemistry of hydrous ringwoodite and water in the Earth's interior, *Phys Earth Planet In*, *143*, 271-278.

Smyth, J. R., D. J. Frost, F. Nestola, C. M. Holl, and G. Bromiley (2006), Olivine hydration in the deep upper mantle: Effects of temperature and silica activity, *Geophys Res Lett*, *33*(15).

Smyth, J. R., N. Bolfan-Casanova, D. Avignant, M. El-Ghozzi, and S. M. Hirner (2014), Tetrahedral ferric iron in oxidized hydrous wadsleyite, *Am Mineral*, *99*(2-3), 458-466.

Smyth, J. R., C. M. Holl, D. J. Frost, S. D. Jacobsen, F. Langenhorst, and C. A. McCammon (2003), Structural systematics of hydrous ringwoodite and water in Earth's interior, *Am Mineral*, *88*(10), 1402-1407.

Song, T. R. A., D. V. Helmberger, and S. P. Grand (2004), Low-velocity zone atop the 410-km seismic discontinuity in the northwestern United States, *Nature*, *427*(6974), 530-533.

Stebbins, J. F., J. R. Smyth, W. R. Panero, and D. J. Frost (2009), Forsterite, hydrous and anhydrous wadsleyite and ringwoodite (Mg_2SiO_4): Si-29 NMR results for chemical shift anisotropy, spin-lattice relaxation, and mechanism of hydration, *Am. Miner.*, *94*(7), 905-915.

Suzuki, A., E. Ohtani, T. Kondo, T. Kuribayashi, N. Niimura, K. Kurihara, and T. Chatake (2001), Neutron diffraction study of hydrous phase G: Hydrogen in the lower mantle hydrous silicate, phase G, *Geophys Res Lett*, *28*(20), 3987-3990.

Thomas, S.-M., S. D. Jacobsen, C. R. Bina, P. Reichart, M. Moser, E. H. Hauri, M. Koch-Müller, J. R. Smyth, and G. Dollinger (2015), Quantification of water in hydrous ringwoodite, *Frontiers in Earth Science*, *2*.

Tsuchiya, J., and T. Tsuchiya (2009), First-principles investigations on the elastic and vibrational properties of hydrous wadsleyite under pressure, *Geochim Cosmochim Ac*, *73*(13), A1350-A1350.

Van der Meijde, M., F. Marone, D. Giardini, and S. van der Lee (2003), Seismic evidence for water deep in earth's upper mantle, *Science*, *300*(5625), 1556-1558.

Vogel, S. C., and H. G. Priesmeyer (2006), Neutron production, neutron facilities and neutron instrumentation, *Neutron Scattering in Earth Sciences*, *63*, 27-57.

Walker, A. M., S. Demouchy, and K. Wright (2006), Computer modelling of the energies and vibrational properties of hydroxyl groups in α and β-Mg_2SiO_4, *Eur J Mineral*, *18*(5), 529-543.

Wilson, C. C. (2000), *Single Crystal Neutron Diffraction From Molecular Materials*.

Ye, Y., R. A. Schwering, and J. R. Smyth (2009), Effects of hydration on thermal expansion of forsterite, wadsleyite, and ringwoodite at ambient pressure, *Am Mineral*, *94*(7), 899-904.

Ye, Y., J. R. Smyth, and D. J. Frost (2011), Structural study of the coherent dehydration of wadsleyite, *Am Mineral*, *96*(11-12), 1760-1767.

Ye, Y., et al. (2012), Compressibility and thermal expansion of hydrous ringwoodite with 2.5(3) wt% H2O, *Am Mineral*, *97*(4), 573-582.

Yoshino, T., G. Manthilake, T. Matsuzaki, and T. Katsura (2008), Dry mantle transition zone inferred from the conductivity of wadsleyite and ringwoodite, *Nature*, *451*(7176), 326-329.

Young, T. E., H. W. Green, A. M. Hofmeister, and D. Walker (1993), Infrared spectroscopic investigation of hydroxyl in β-$(Mg,Fe)_2SiO_4$ and coexisting olivine - Implications for mantle evolution and dynamics, *Phys. Chem. Miner.*, *19*(6), 409-422.

Yusa, H., and T. Inoue (1997), Compressibility of hydrous wadsleyite (beta-phase) in Mg_2SiO_4 by high pressure X-ray diffraction, *Geophys Res Lett*, *24*(14), 1831-1834.

Yusa, H., T. Inoue, and Y. Ohishi (2000), Isothermal compressibility of hydrous ringwoodite and its relation to the mantle discontinuities, *Geophys Res Lett*, *27*(3), 413-416.

Zha, C. S., T. S. Duffy, H. K. Mao, R. T. Downs, R. J. Hemley, and D. J. Weidner (1997), Single-crystal elasticity of β-Mg_2SiO_4 to the pressure of the 410 km seismic discontinuity in the Earth's mantle, *Earth and Planetary Science Letters*, *147*(1-4), E9-E15.

Zikovsky, J., P. F. Peterson, X. P. P. Wang, M. Frost, and C. Hoffmann (2011), CrystalPlan: an experiment-planning tool for crystallography, *J Appl Crystallogr*, *44*, 418-423.